2014

Ordered supramolecular oligothiophene structures on passivated silicon surfaces

Liu, Renjie

ORDERED SUPRAMOLECULAR OLIGOTHIOPHENE STRUCTURES ON PASSIVATED SILICON SURFACES

BY

Renjie Liu

A thesis submitted in partial fulfillment of the requirements
for the degree of Master of Science
Department of Physics
Lakehead University

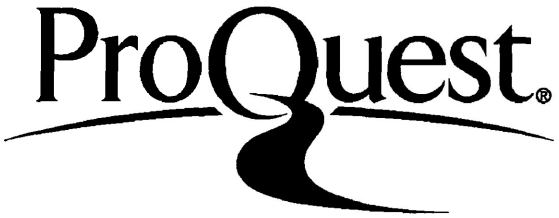

ABSTRACT

The adsorption of brominated tetrathienoanthracene molecules (TBTTA) onto the Si(111) $\sqrt{3}\times\sqrt{3}$-Ag surface has been studied. The molecules were absorbed at room temperature and annealed up to 400°C. One monolayer of Ag was used to passivate the Si surface. Evidence provided by the scanning tunneling microscope (STM) images indicates that at low coverage the molecules readily form 2-d structures. Many images show direct evidence of molecular mobility at room temperature. With increasing coverage the molecules eventually form compact supramolecular structures. In terms of the $\sqrt{3}$ lattice vectors ($\boldsymbol{a'}$ and $\boldsymbol{b'}$), we can define an incommensurate unit cell with $\boldsymbol{a} = 0.85\boldsymbol{a'} + 2.6\boldsymbol{b'}$ and $\boldsymbol{b} = 2\boldsymbol{a'} + \boldsymbol{b'}$ and an internal angle of $\alpha = (70 \pm 2)°$. Allowing for measurement error the closest commensurate structure consistent with our measurements is: $\boldsymbol{a} = \boldsymbol{a'} + 2\boldsymbol{b'}$ and $\boldsymbol{b} = 3\boldsymbol{a'} + \boldsymbol{b'}$. We have found that this structure is quite fragile and can decompose under STM imaging at high bias ($> |2|$ *V*) and low bias conditions ($< |0.7|$ *V*). Our results suggest that TBTTA is weakly bound to the $\sqrt{3}$ surface at room temperature and the supramolecular structures are held together by weak van der Waals forces. At high coverage, another ordered structure is observed. The structure is a 1-d chain like structure, with a periodicity along the chain of (9.5 ± 0.5) Å. We have also studied the effect of annealing the TBTTA structures. No ordered structures were observed at temperatures ranging from 425°C to 160°C. At 145°C, we found ordered structures. The structures appear to contain two parallel chains, with a third row in some cases. The periodicity along the chains measures (10 ± 0.5) Å and the distance between similar features in adjacent chains is also (10 ± 0.5) Å. The chain direction is rotated by (30 ± 2)° with respect to the $\sqrt{3}$ direction. We also find that these structures are more robust under STM scanning under different bias conditions.

TABLE OF CONTENTS

CHAPTER 1 Introduction

Motivated by possible applications in electronics and sensor technology, the fabrication of non-conjugated surface-supported organic structures has attracted a great deal of attention for a number of years (Bartels 2010; Champness 2007; El Garah et al. 2013; Franc & Gourdon 2011; Gourdon 2008; Grill et al. 2007; Lackinger & Heckl 2011; Palma & Samori 2011). In particular, the functionalization of semiconductor surfaces with organic molecules is a necessary step to develop hybrid organic-semiconductor devices. A significant challenge to functionalization is the fact that many semiconducting surfaces exhibit a large amount of dangling bonds that can suppress the diffusivity of organic molecules. Diffusivity is suppressed due to the formation of Si-C bonds (Carbone et al. 1998) which can lead to rehybridization and loss of aromaticity of the adsorbed molecules.

Recently, Suzuki et al. (2009) demonstrated that these problems can be overcome by depositing the organic molecules onto a passivated semiconducting surface. These authors used one monolayer of silver to form a Si(111) $\sqrt{3}\times\sqrt{3}$-Ag surface which has no dangling bonds. They demonstrated that this substrate can provide a surface with high mobility, and is suitable for the formation of supramolecular structures. Suzuki et al. (2009) formed an ordered layer of terephthalic acid (TPA) on the $\sqrt{3}$-Ag surface. They found that the structure of this molecular layer is similar to TPA layers formed on Ag(111) single crystal metal surfaces. In contrast, when they deposited TPA onto the bare Si(111) 7×7 surface no ordered molecular structures were observed due to large covalent molecule-substrate interactions.

In this thesis we chose to study the deposition of Tetrabromo-tetrathienoanthracene (TBTTA) molecules on the $\sqrt{3}$-Ag surface. TBTTA is a thiophene-based molecule of considerable interest in organic semiconductor research (McCullough 1998) due to the efficient conjugation and chemical stability of the monomer. In thin film form, thiophene layers exhibit reasonable mobility, i.e. diphenyl(dibenzothienothiophene)

has $\mu_h = 2.0\ cm^2\ V^{-1}\ s^{-1}$ (Takimiya et al. 2006). In addition to non-conjugated layers, thiophene based molecules have also been used as precursors in a number of surface-confined polymerization experiments. In these experiments Ullman polymerization of halogenated thiophene molecules was used to form extended conjugated oligomers on single crystal noble metal surfaces (Gutzler et al. 2014). The long-term goal of our work is to identify a semiconducting or insulating surface suitable for surface confined polymerization experiments.

In surface-confined polymerization multi-dentate monomers are deposited onto an atomically flat surface to confine the polymerization reaction epitaxially, and produce polymers with a high degree of order and electronic conjugation in 2-d. A number of "proof-of-principle" studies have been reported; yet, the formation of regular 2-d surface-confined polymers remains a challenge (Bieri et al. 2010; Cai et al. 2010; Gutzler et al. 2014; Perepichka & Rosei 2009). Most of the surface-confined experiments reported so far have been performed on conducting substrates, yet many of the useful properties of these 2-d conjugated layers can only be exploited if the layers are formed on insulating or semiconducting substrates. The long-term goal in our research group is to form covalent organic molecular structures with conjugation in 2-d on semiconducting or insulating substrates. The first step is to find a suitable semiconducting substrate, and the experiments outlined in this thesis represent this first step.

In this thesis we study the deposition and ordering of TBTTA, onto the Si(111) $\sqrt{3}\times\sqrt{3}$-Ag surface using Scanning Tunneling Microscopy (STM), low energy electron diffraction (LEED), and Auger electron spectroscopy (AES). The primary goal of the research is to investigate whether or not the $\sqrt{3}$-Ag surface provides suitable mobility for TBTTA monomers, and if so to study nature of any adsorbed structures.

The thesis is organized as follows: Chapter 2 outlines the properties of our silicon substrate and the $\sqrt{3}$ silver overlayer; Chapter 3 discusses the experimental techniques utilized and sample preparation; Chapter 4 is devoted to results and discussions; and the conclusions are presented in chapter 5.

CHAPTER 2 Background

2.1 Silicon Crystallography

Silicon is one of the most widely used semiconducting substrates. Silicon single crystals are 'face-centered-cubic' (fcc) with a basis of 2 atoms. The primary cleavage plane is the (111) plane as outlined in blue in Figure 2.1.

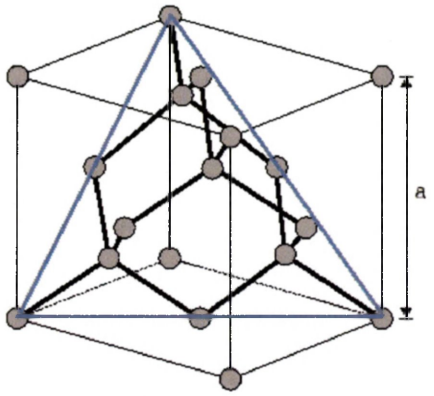

Figure 2.1. The (111) plane of a silicon crystal.

When a clean (111)-oriented surface of Silicon is heated to sufficiently high temperatures (at least 400° C), and under ultra-high vacuum (UHV) conditions, the surface atoms rearrange into the lowest energy 7×7 configuration which is stable at room temperature. The first comprehensive structural analysis of the Si(111) 7x7 surface reconstruction was performed by evaluating the intensity distribution of the spots in transmission electron diffraction patterns (Takayanagi et al. 1985) and led to the dimer-adatom-stacking-fault (DAS) model.

Each supercell in the DAS model of the 7x7 reconstruction consists of three layers (see Figure 2.2). The top layer contains 12 atoms (the so called adatoms); the second layer is the rest atom layer with 42 atoms, and 48 atoms are in the third layer that contains a stacking fault. Of all the surface atoms involved in the reconstruction, 19 are threefold coordinated and possess dangling bonds. In particular, there are 12 adatoms, 6 rest atoms and 1 atom in the center of the corner hole.

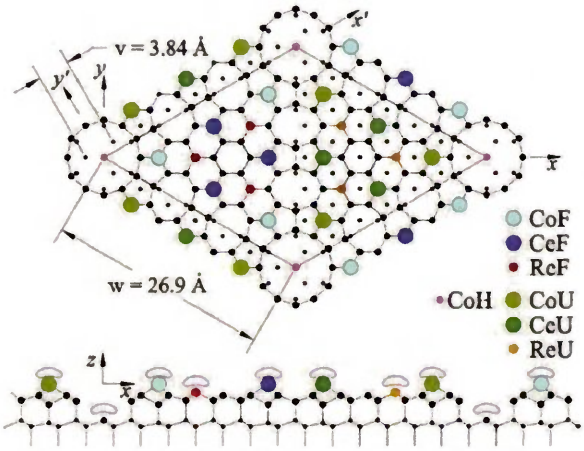

Figure 2.2. The adatoms in the DAS model fall into four symmetry classes: corner faulted (CoF), center faulted (CeF), corner unfaulted (CoU), center unfaulted (CeU). The 19 dangling bonds occur at 12 adatoms, 6 rest atoms (ReF, ReU) and the atom in the center of the corner hole (CoH). Graph reproduced from Giessibl et al. (2001).

2.2 Si (111) √3×√3 R30°- Ag Surface

Even though the 7x7 reconstruction reduces the dangling bond density from 49 to 19 dangling bonds per 7x7 unit cell, research indicates that many organic molecules deposited on this surface are not mobile enough to form ordered domains but absorb randomly and "hit and stick" (Brown et al. 1998). As discussed by Suzuki et al. (2009) one way to increase the diffusivity of organic molecules on the Si surface is to introduce a monolayer of silver. It is generally accepted that the √3×√3 reconstruction is obtained following the deposition of one monolayer of silver at a substrate temperature of 600°C. One monolayer (1ML) is defined here as 7.83×10^{14} Ag atoms/cm^2. One popular structural model for Si(111) √3×√3-Ag surface is the honeycomb-chained-triangle (HCT) model (Takahashi et al. (1988); Takahashi et al. (1991); Takahashi and Nakatani (1993)). According to the HCT model, a monolayer of silver atoms leads to the formation of the silicon trimers such that every Si atom at the surface is 4-fold coordinated and therefore there are no Si dangling bonds (Figure 2.3).

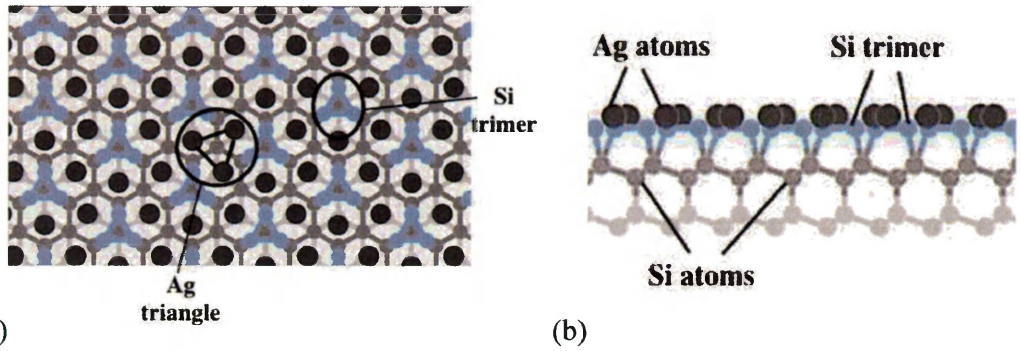

Figure 2.3. (a) A top view of Ag - √3×√3 structure on the Si(111) surface, and (b) a side view of the silicon trimers with Ag atoms on the top layer.

In the Figure 2.4, we show a schematic of the atomic arrangement of the √3-Ag reconstruction and an STM image of this surface. The highly ordered 2-d hexagonal structure can be observed in the image.

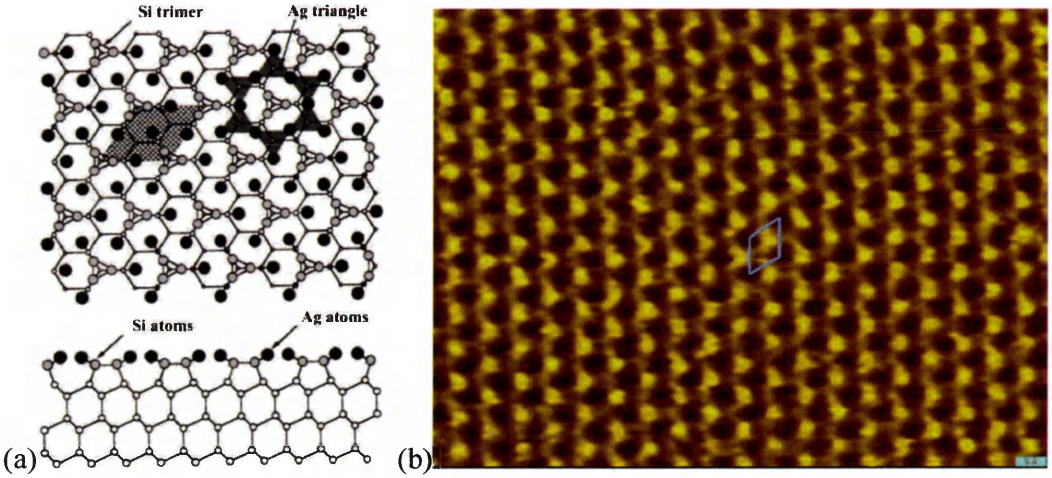

Figure 2.4. (a) The atomic structure of √3-Ag reconstruction, with hexagonal unit cell shaded. Figure reproduced from Tong et al. (2002). (b) A 100Å×100Å STM image of the √3-Ag surface with unit cell highlighted in blue.

2.3 Molecular Deposition

2.3.1 Classification of Overlayer Structures

In the case of overlayers and molecular deposition, it is important to understand the relationship between the arrangement of the layer with respect to the substrate. Here

we state the two principal methods for specifying the structure: Wood notation and matrix notation.

(1) Wood Notation

Wood notation is the simplest and most frequently used method for describing a surface structure. However, it works only when the included angles of the surface and substrate unit cells are the same.

In essence, Wood notation involves specifying the lengths of the two overlayer vectors, ***a'*** and ***b'***, in terms of ***a*** and ***b***, which are primitive vectors of the bulk terminated surface. This can be written in the format $|a'| = p|a|$ and $|b'| = p|b|$ with a unit cell rotation of ϕ. Thus, the overlayer structure is referred to as:

$$(p \times q)R\phi° \qquad (2\text{-}1)$$

i.e. the way we describe the one monolayer of silver on Si(111) using this form is Si(111) $\sqrt{3}\times\sqrt{3}$ R30°-Ag, which mean the length of vectors for Ag overlayer are $\sqrt{3}$ times over the length of the bulk terminated Si vectors; and the angle between the two unit cells is 30°. (see Figure 2.5)

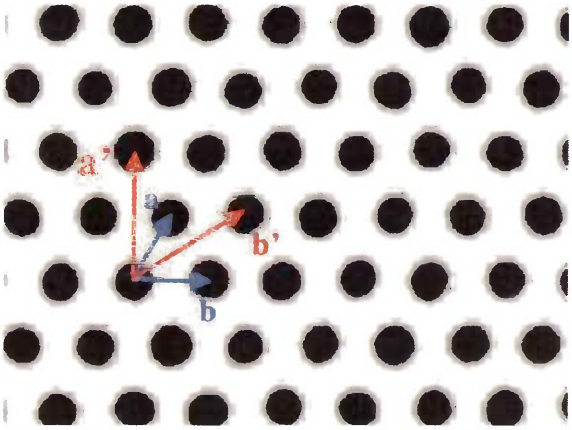

Figure 2.5. A schematic of relationship between √3 – Ag unit vectors (***a'*** and ***b'*** in red) and Si(111) bulk terminated unit vectors (***a*** and ***b*** in blue).

(2) Matrix Notation

Alternatively if the lattice vectors of the bulk terminated surface are ***a*** and ***b***, and the

unit cell of the overlayer are defined by ***a'*** and ***b'*** then the relationship between the two lattices can be expressed by a matrix:

$$\begin{bmatrix} a' \\ b' \end{bmatrix} = [C] \begin{bmatrix} a \\ b \end{bmatrix} = \begin{bmatrix} p & q \\ r & s \end{bmatrix} \begin{bmatrix} a \\ b \end{bmatrix} \quad (2\text{-}2)$$

Where [C] is the transformation matrix (Woodruff & Delchar 1994). With this matrix, the epitaxial relationship between the substrate and molecular layer can be classified into one of three categories; commensurate, coincident, or incommensurate. In the case of commensurate structures, all the overlayer lattice points coincide with symmetrically equivalent substrate points and therefore all the elements for $\begin{bmatrix} p & q \\ r & s \end{bmatrix}$ are integers. In case of coincident epitaxy, it demands the *p, q, r, s* elements in the matrix are rational fractions with a magnitude > 1 (Wiesendanger 1994). In incommensurate structures there is no epitaxial relationship between the substrate lattice and the adsorbate lattice (Hooks et al. 2001). Take the relationship in Figure 2.5 as an example. With unit vectors for Si(111) surface ***a***, ***b***, the Ag-$\sqrt{3}$ overlayer vectors ***a'***, ***b'*** can be expressed in matrix form:

$$\begin{pmatrix} a' \\ b' \end{pmatrix} = \begin{pmatrix} 2 & -1 \\ 1 & 1 \end{pmatrix} \begin{pmatrix} a \\ b \end{pmatrix} \quad (2\text{-}3)$$

Molecular epitaxy is more complicated compared with atomic epitaxy. With organic molecules, additional parameters must be considered. The most fundamental difference between the growth of atomic and molecular systems is that organic molecules have internal degrees of freedom. Moreover, the size of the molecules and thus the associated unit cells are large which can contribute to an additional source of disorder.

2.3.2 TBTTA Molecules

Halogen terminated molecules have been widely studied as attractive candidates in monolayer formation experiments both at the liquid-solid interface and under UHV conditions on different substrates (Chung et al. 2011; Clarke et al. 2011; Schlogl et al. 2011; Walch et al. 2010; Yoon et al. 2011). TBTTA is a thiophene based organic molecule with four thiophene rings at the four corners of the molecule (Figure 2.6). The deposition of TBTTA onto Cu(111), Ag(111), Cu(110), and Ag(110) (Gutzler et al.

2014) surfaces has been investigated. Covalent networks were observed on both Cu and Ag surfaces. In addition to experiments on metal surfaces another experiment investigated TBTTA layers at the solid–liquid interface on highly oriented pyrolytic graphite (HOPG) (Gutzler et al. 2012).

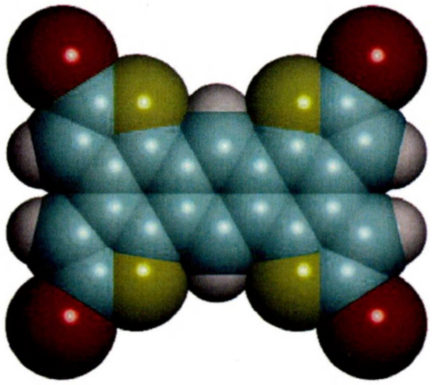

Figure 2.6. The Molecular structure of TBTTA. Bromine atoms are indicated in red, Carbon atoms in blue, Sulfur atoms in yellow, and hydrogen atoms in white.

The TBTTA monomers used in this work were synthesized and supplied by Prof. Dmitrii Perepichka's group in the Chemistry Department at McGill University. The monomers were synthesized using Stille Coupling of 2- and 3-(tributylstannyl) thiophene derivatives with tetrabromobenzene followed by an oxidative cyclization as reported by Brusso et al. (2008).

2.3.3 Molecular Organization

Figure 2.7 shows the elementary processes involved during molecular deposition, which consists of adsorption, inter-layer diffusion, nucleation and dissociation. Desorption is possible but highly unlikely on our surface at room temperature.

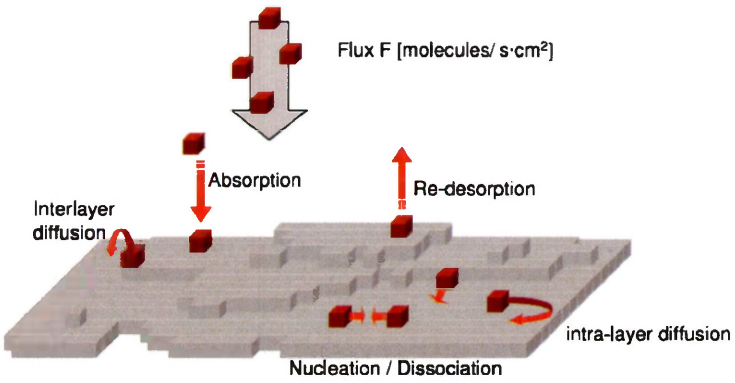

Figure 2.7. Schematic of processes relevant to organic molecular deposition. Such as adsorption, re-adsorption, intra-layer diffusion (on a terrace), inter-layer diffusion (across steps), nucleation and growth of islands. Graph from Kowarik et al. (2008).

There are two types of molecular adsorption. One is physical adsorption or physisorption, which refers to the case when there is no electron transfer between the molecules and the substrate. In this instance the molecule-substrate interaction is usually of van der Waals type (Umbach et al. 1996). Another one is chemical adsorption, which refers to the case when electron transfer or sharing, i.e. covalent bonding occurs between an adsorbed molecule and the surface atoms.

In the case of physisorption the monomers can diffuse quite readily on the surface and can nucleate 2-d islands or adsorb to an existing island. However, at finite temperature there is also a non-zero probability of dissociation of a monomer from the island into the molecular "gas" on the surface.

CHAPTER 3 Experimental Techniques

3.1 Instrumentation

3.1.1 UHV System

Ultra-high-vacuum (UHV) conditions are necessary for our experiment for two specific reasons. First, the silicon substrate surface is highly reactive and not stable in an ambient environment. The UHV system can reduce the contamination from background gases by reducing the number of molecules impinging on the surface. Second, vacuum is required to permit the use of low energy electron techniques without undue interference from gas phase scattering.

Monolayer formation time is defined as the time needed to form a single layer of molecules on a surface assuming that every molecule that strikes and sticks and the molecules distribute to form a single atomic layer. Considering a cube of length a. The total area of the cube faces is $6a^2$ and the volume is a^3. With a gas density (n) and average velocity $\langle v \rangle$, the collisions with the walls per second can be written as:

$$(na^3)\left(\frac{\langle v \rangle}{a}\right) = na^2\langle v \rangle \tag{3-1}$$

So the rate of arrival for atoms or molecules per unit area per second on one of the cube faces can be written as:

$$Z(\text{molecules}/\text{cm}^2/\text{s}) = \frac{1}{6}n\langle v \rangle \tag{3-2}$$

Using the kinetic theory of the gas, Equation (3-2) can be rewritten as:

$$Z = 3.51 \times 10^{22}\frac{P}{\sqrt{MT}} \tag{3-3}$$

Where P is the pressure in Torr, M is molecular weight in g/mole, and T is the temperature in Kelvin. At ambient temperature for air ($M=29$):

$$Z = 3.77 \times 10^{20}P \tag{3-4}$$

Assuming each nitrogen molecule occupies an area on the surface of d_0^2 (where $d_0 = 0.372\ nm$ for air) then the atomic flux can be written as:

$$Z \cdot d_0^2 = Z/s = 5.2 \times 10^5 P \tag{3-5}$$

Given that the monolayer formation time is just the inverse of the atomic flux:

$$T_{ml} = \frac{1}{Z \cdot d_0^2} = 1.9 \times 10^{-6}/P \qquad (3\text{-}6)$$

At ambient temperature, the monolayer formation time for air is *19,000 s* (*5.3 hrs*) in our UHV system ($P \sim 10^{-10}\ Torr$). This is an acceptable value for our experiments and compares with only *1.9 s* in a high vacuum system ($10^{-6}\ Torr$) and *2 ns* at atmospheric pressure ($760\ Torr$).

Our UHV system contains four pumps, a residual gas Analyzer, two evaporators (a metal and a molecular evaporator), a low energy electron diffraction instrument, an Auger electron spectrometer and a scanning tunneling microscope. A schematic of the vacuum system used in this experiment is shown in Fig. 3.1.

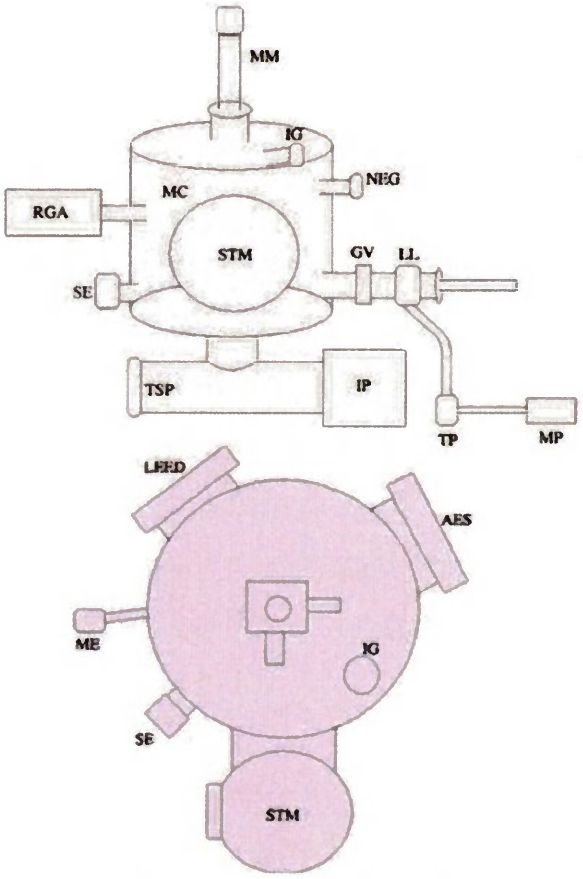

- IG: Ion Gauge
- MC: Main Chamber
- NEG: Non-evaporable Getter pump
- RGA: Residual Gas Analyzers
- STM: Scanning Tunneling Microscope
- SE: Silver Evaporator
- GV: Gate Valve
- LL: Load Lock
- TSP: Titanium Sublimation Pump
- IP: Ion Pump
- TP: Turbomolecular Pump
- MP: Mechanical Pump
- AES: Auger Electron Spectrometer
- LEED: Low Energy Electron Diffraction
- ME: Molecular Evaporator

Figure 3.1. A schematic of our UHV system.

3.1.2 Vacuum Pumps

Four pumps are used in combination to maintain the base pressure inside the chamber. The first pump is a turbomolecular pump, and a mechanical pump for backing. This pump combination is used for initial chamber pump down and to pump the fast entry load lock. The turbomolecular pump works on the principle of momentum transfer. High-speed rotating blades transfer momentum to the gas molecules, and the relative velocity between slotted rotating blades and slotted stator blades transports the gas molecules from inlet flange to the outlet. Usually pumps are designed with multiple blades and multiple stages. There are two parameters that characterize the performance of the pump. The first is the maximum compression ratio, which is defined as the ratio of outlet to inlet pressure with no gas flow. Another is the maximum pumping speed, which is defined as the flow rate of a gas at the inlet when the compression ratio across the blades is unity. The ultimate pressure for a turbomolecular pump is determined by the compression ratio for the light gases (usually hydrogen) and the outgassing rate of the metal parts.

Turbomolecular pumps work most efficiently in the molecular flow regime (below 10^{-4} Torr), where the mean free path of the molecules is limited only the dimensions of the vacuum enclosure. This is the reason a mechanical pump is required for backing. The mechanical pump compresses gases using a rotor and vane in the pumping chamber and then expels the gas to the atmosphere. The turbomolecular pump we use in our laboratory is a Varian Turbo-V60[1], which has a compression ratio of 5×10^7 and a pumping speed of 65 L per second for nitrogen. The ultimate pressure for this pump is 8×10^{-10} Torr. We also use an Edwards E2M2 mechanical pump[2] for backing.

The primary pump in our system is an ion pump. An ion pump operates on the principle of Penning cold-cathode discharge (Landauer 1962). A diode sputter-ion

[1] Varian, Inc. http://www.varianinc.com
[2] BOC Edwards. http://www.bocedwards.com

pump generally consists of an anode, two cathodes and a magnet. During operation, high-energy electrons emitted from the cathode elements collide with and ionize gas molecules which are accelerated to the cathode. Due to the presence of both electric and magnetic fields in each cell, electrons travel in helical orbits, which increases the path length before they reach the anode. This improves the chances of electron collision with the gas molecules inside the Penning cell. Ionized gas molecules are accelerated to the titanium cathode and many are buried. The ions may also sputter titanium and can produce secondary electrons. The sputtered Ti is deposited on nearby surfaces to getter active gases. Titanium is a very reactive metal, so the sputtered Ti can chemically combine with any active gas molecules present (e.g. CO, CO_2, H_2, N_2, O_2) to form stable compounds, thus removing them from the vacuum vessel. The ion pump in our system is a Varian, VacIon Plus 150[3] with an ultimate pressure of 10^{-11} *Torr*, and a pumping speed of *150 L* per second for nitrogen.

In addition to the ion pump we used two getter pumps to achieve our base pressure; a titanium sublimation pump (TSP), and a non-evaporable getter pump (NEG). The TSP sublimates a fresh layer of titanium onto a relatively large surface. As in the ion pump the titanium layer has a high pumping speed for reactive gases, which either form a chemical compound or are adsorbed. The Ti layer has a finite lifetime and therefore regular deposition is required to maintain the pumping efficiency. Normally, at UHV pressures a fresh titanium film can continue to be effective for at least *24 hrs*.

The NEG pump is a Capacitor-D400 NEG pump[4]. Like the TSP the NEG pumps by chemisorbing active gases. For the NEG this is followed by bulk diffusion. The NEG is made from a sintered porous material (St 172 (Zr-V-Fe)), and when the pump is saturated it can be reactivated by heating the getter material to a temperature in the range of 150°C – 300°C.

[3] Varian, Inc. http://www.varianinc.com
[4] SAES Getters, S.P.A, http://www.seasgetters.com

In addition to the pumps mentioned an extra step is required to attain UHV pressures. This step is called baking. When the vacuum system is exposed to ambient pressure, a lot of gas molecules are absorbed into the walls of the vacuum chamber. When the pressure is reduced, these molecules desorb. The predominant gas desorbing from an unbaked system is water vapor. The ultimate pressure of the system represents equilibrium between the pumping speed of the system and the outgassing rate of the inner walls and the components inside the chamber. Baking actually works to accelerate this outgassing by heating the entire system. The so-called bakeout procedure is to heat entire UHV system to a high temperature, typically higher than 100 degrees Celsius for several days, so as to eliminate water vapor on cool down. An ultimate pressure after baking of less than 1×10^{-10} Torr can be achieved.

3.1.3 Low Energy Electron Diffraction (LEED)

Low Energy Electron Diffraction is one technique we used to investigate the surface structure of our samples. In a LEED experiment an electron beam is coherently reflected from the sample surface to form a diffraction pattern on a phosphor screen. In a typical diffraction pattern, we are interested in the bright spots produced by constructive interference from the surface atoms. The position of these bright spots provides information on the size, symmetry and rotational alignment of the 2-dimensional surface net of atoms on the crystal surface.

According to the de Broglie relation, the wavelength and the momentum of the electrons can be related by the following equation:

$$\lambda = \frac{h}{p} \tag{3-7}$$

Where p is the electron momentum and can be represented non-relativistically as:

$$p = m \cdot v = \sqrt{2m(K_E)} = \sqrt{2meV} \tag{3-8}$$

Where m is the mass of the electron, v is velocity, K_E is kinetic energy, e is electronic charge and V is the acceleration voltage. Using the Equation (3-7) and (3-8), the wavelength for the electron can be written as:

$$\lambda = \frac{h}{\sqrt{2meV}} \quad (3\text{-}9)$$

A LEED instrument has a low energy electron gun that can produce electrons of a kinetic energy ranging from 20 eV-100 eV. At these energies the mean free path for electrons is sufficiently short that they can only penetrate two or three atomic layers into the surface (5-10 Å), and therefore the LEED pattern contains information on the surface atoms rather than the structure of the bulk.

The diffraction condition can be visualized in a graphical way by means of the Ewald sphere construction. The Ewald sphere is a geometric construct that demonstrates the relationship between the wavevector of the incident and diffracted x-ray beams. Assuming $\boldsymbol{a}$, $\boldsymbol{b}$ and $\boldsymbol{c}$ are the lattice vectors for the 3-dimensional unit cell at the crystal surface, the corresponding reciprocal lattice vectors $\boldsymbol{a}^*$, $\boldsymbol{b}^*$ **and** $\boldsymbol{c}^*$are given by (Woodruff & Delchar 1994):

$$a^* = 2\pi\frac{b\times c}{V} \quad b^* = 2\pi\frac{a\times c}{V} \quad c^* = 2\pi\frac{a\times b}{V} \quad V = a\cdot b\times c \quad (3\text{-}10)$$

To obtain a 2-d reciprocal lattice for a surface, let the base vector $\boldsymbol{c}$ approach infinity with the $\boldsymbol{a}$ and $\boldsymbol{b}$ vectors unchanged. As a result, the corresponding reciprocal lattice vector $\boldsymbol{c}^*$ approaches 0. The discrete points parallel to $\boldsymbol{c}^*$ in the reciprocal lattice coalesce to form lines or rods as shown in Figure 3.2, and the three dimensional reciprocal lattice vector g_{hkl} reduces to g_{hk} in 2-d defined by:

$$g_{hk} = ha^* + kb^* \quad (3\text{-}11)$$

To a first approximation the LEED pattern is a Fourier transform of the real space surface lattice. We can define the incident wavevector of the electron as k and the emerging wavevectors as k'. For elastic scattering:

$$k^2 = k'^2 \quad (3\text{-}12)$$

We can also define the component of the wavevector parallel to the surface as $k_{\parallel}$, and the component perpendicular to the surface as $k_{\perp}$. The reciprocal lattice of a surface is a 2D lattice with rods extending perpendicular to the surface from each lattice point. The rods can be pictured as regions where the reciprocal lattice points are infinitely dense. So the condition for momentum conservation and constructive interference for

2-d diffraction becomes:

$$k'_{\parallel} = k_{\parallel} + g_{hk} \qquad (3\text{-}14)$$

An adapted version of the Ewald sphere construction can be used to represent Equation (3-14). Using the origin of k as the center of the sphere, a sphere of radius $2\pi/\lambda$ is constructed in reciprocal space.

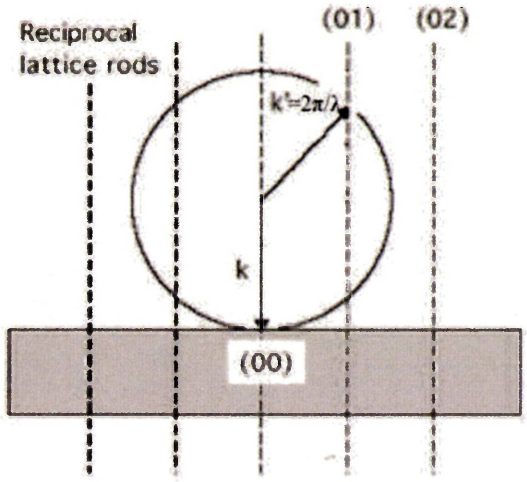

Figure 3.2. The Ewald sphere within the 2-d reciprocal lattice.

Constructive interference and a diffracted beam occurs wherever a reciprocal lattice rod intersects the surface of the Ewald sphere. The diffracted pattern thus reflects the symmetry of the surface unit cell.

For example, deposition of a monolayer of silver onto a clean Si(111) 7×7 surface held at 600°C results in a $\sqrt{3}\times\sqrt{3}$ R30° diffraction pattern as observed in Figure 3.3.

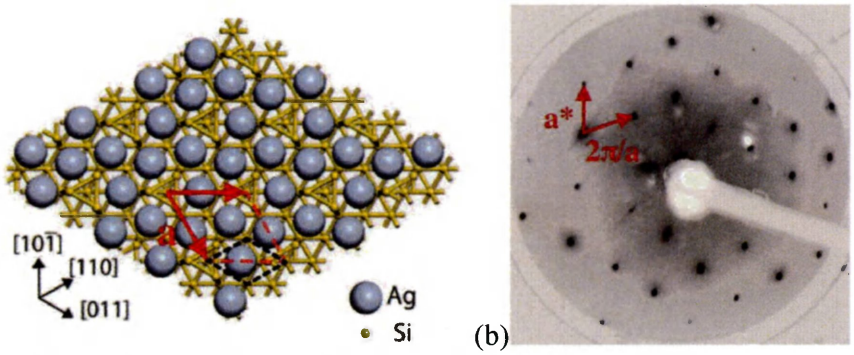

Figure 3.3. (a) Si (111) √3×√3 – Ag R30 degree reconstruction in real space. ***a*** is one of the unit vectors for √3 – Ag layer with a length of *a*. Graph reproduced from Murphy et al. (2012). (b) LEED diffraction pattern. ***a**** is the one the unit vectors in reciprocal space lattice vectors, with a length of $2\pi/a$.

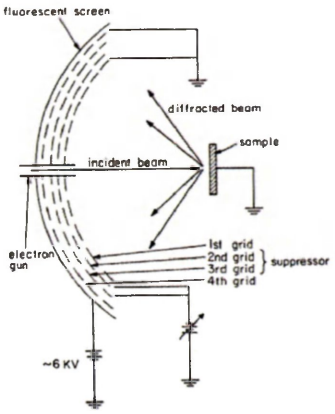

Figure 3.4. A LEED schematic diagram. Reproduced from *Low-Energy Electron Diffraction: Experiment, Theory and Surface Structure Determination* (VanHove et al. 1986).

A schematic diagram of the LEED used in our laboratory is show in Figure 3.4. An incident electron beam is produced by a tungsten filament and focused by a series of electrostatic lenses. The first grid of the screen and the last electrode of the electron gun are at the same potential as the sample, so that a field-free space is created for the incident and backscattered electrons to travel. The backscattered electrons are collected by a series of hemispherical grids. After the first grid, the second and third grids produce a retarding potential to reject any inelastically scattered electrons that contain no diffraction information. The elastically scattered electrons pass though the retarding field and are then accelerated by the fourth grid to the fluorescent screen to produce the observed diffraction pattern. The pattern is recorded by a

computer-controlled video camera purchased from Electrim Corporation[5].

3.1.4 Auger Electron Spectroscopy (AES).

(1) Auger Process

Auger electron spectroscopy is an analytical technique which provides information on the elemental makeup of the surface. An Auger process starts with an election being ejected by an incident electron (or X-ray) beam to form a vacancy in an otherwise occupied level. To fill the vacancy a second electron from a higher orbital will fall into this state. To conserve energy, two possible processes can take place. The first is radiative via the emission of an x-ray photon, and the second is nonradiative process, involving two electrons with one of these electrons (the Auger electron) ejected from the sample carrying the excess energy. (see Figure 3.5) The process illustrated in Figure 3.5 is a KL_2L_3 transition given the three electron energy levels involved.

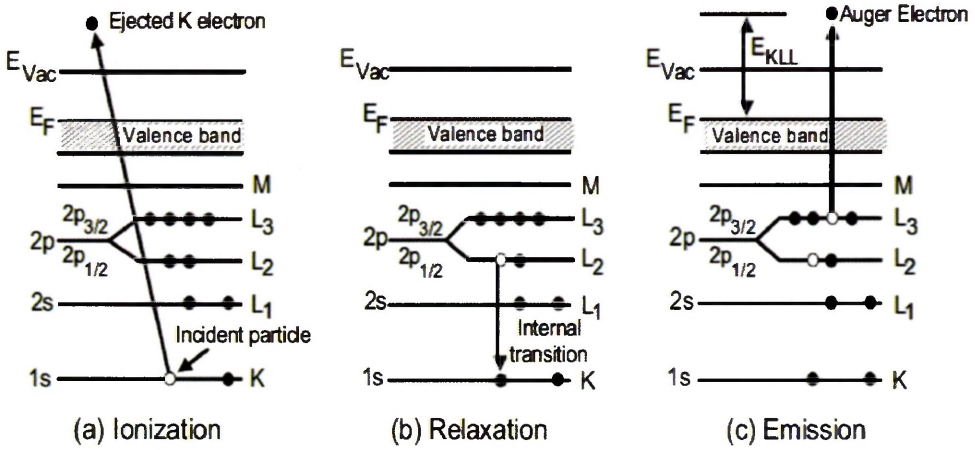

Figure 3.5. A schematic diagram of (a) the ejection of a k-shell electron followed by (b) and (c) a KL_2L_3 Auger transition. Graph reproduced from *Handbook of Auger Electron Spectroscopy* (Hedberg 1995).

[5] Electrim Corporation http://www/electrim.com

(2) Characteristic Auger Electron Energies

The kinetic energy of an Auger electron is approximately the energy difference between the energy lost by the electron making the transition into the vacancy and the energy of the electron shell from which the Auger electron was ejected. Let E_a, E_b and E_c be the binding energy of electrons in a, b and c levels of the neutral atom respectively. Hence, the kinetic energy of this Auger electron can be expressed as

$$KE = E_a - E_b - E_c - U \tag{3-15}$$

Here, $E_a - E_b$ is the energy lost by the relaxed electron and E_c is the initial binding energy of the Auger electron. U lumps together the hole-hole interaction energy in the final state, and any screening, polarization and relaxation energies (Woodruff & Delchar 1994). From Equation (3-15), we see that the Auger electron has a discrete energy characteristic of the three energy levels involved for a specific atomic species. Based on these characteristic energy levels we can make spectroscopic identification of the element. For example, the Auger transition energy for the Si KLL transition is:

$$E_{KLL} \approx E_k - E_{L_1} - E_{L_{23}} \tag{3-16}$$

Due to the short mean free path of the relatively low energy Auger electrons, AES is a surface sensitive technique. Although atomic excitations can take place ~ 10,000 Å below the surface, only Auger electrons within a depth of several Ångstroms are actually ejected without energy loss.

(3) Instrumentation and Spectra

The Auger spectrometer in our laboratory is an Omicron CMA 100[6]. The spectrometer includes an integrated electron gun with a tungsten filament to provide a 3000 eV electron beam. The electron analyzer is a Cylinder Mirror Analyzer (CMA). The CMA consists of two coaxial cylinders with a negative potential applied to the outer cylinder and ground potential applied to the inner cylinder. When the electron beam hits the sample, backscattered electrons which enter the CMA cylinder will be repelled by the negative potential on the outer cylinder and only electrons with the

[6] Omicron NanoTechnology GmbH. http://www.omicron.de

selected or "pass" energy will enter through a second aperture on the inner cylinder to the analyzer. During the scanning process, the electron current as a function of "pass" energy is recorded and Auger transitions are measured.

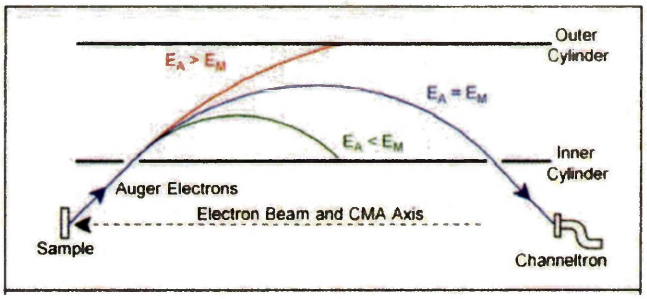

Figure 3.6. A schematic diagram for energy selectivity of the upper half of a cross section of a CMA. Reproduced from *Handbook of Auger Electron Spectroscopy* (Hedberg 1995).

In addition to Auger electrons the measured electron current also includes contributions from secondary and backscattered electrons, and thus can result in small, broad Auger peaks. For this reason rather than plotting the number of electrons emitted as a function of the kinetic energy, N(E), it is more common to plot the first derivative dN(E)/dE. Figure 3.7 (b) is an example of Auger spectrum plotted using dN(E)/dE. With this plotting mode, Auger transitions peaks are sharper and better defined.

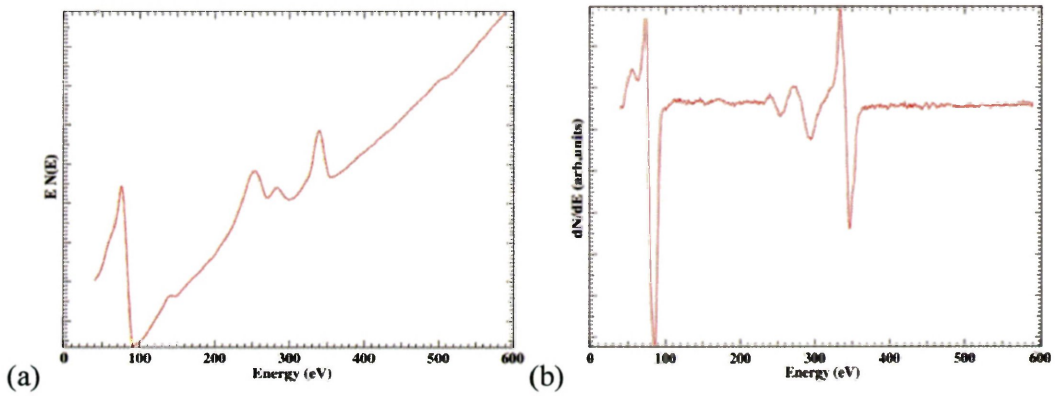

Figure 3.7. An Auger spectrum for one monolayer of Ag on Si(111) plotted as (a) intensity vs. energy and (b) the derivative dN/dE vs. energy.

3.1.5 Scanning Tunneling Microscopy

The scanning tunneling microscope (STM) was developed by Binnig and Rohrer (1986) at IBM. When a metal tip is brought extremely close to a conducting surface, electrons can quantum mechanically tunnel from one to the other. The probability of tunneling is exponentially dependent on the distance. The topography of the surface can be mapped out by keeping the tunnel current constant as the tip is rastered across the surface and measuring the height of the tip. In fact with a sharp enough tip, atomic scale resolution can be obtained.

As stated, the operation of an STM is based on quantum tunneling. In classical physics, particles with an energy less than a potential energy barrier are confined, however quantum mechanics predicts that if the mass of the object is small enough, and the barrier is thin enough, there is a finite probability that the electron will traverse the barrier. If we decribe the electron using a wave function, the decaying solution for the electron wave function inside a rectangular barrier with a width ***d*** can be expressed as:

$$\Psi(d) = \Psi(0)e^{-\kappa d} \tag{3-17}$$

The probablity of finding an electron beyond the barrier is

$$|\Psi(d)|^2 = |\Psi(0)|^2 e^{-2\kappa d} \tag{3-18}$$

where:

$$\kappa = \frac{\sqrt{2m(V-E)}}{\hbar} \tag{3-19}$$

here V is the height of the barrier and E is the energy of the electron.

In the case of STM, the vacuum space between the sample and tip acts as the potential barrier between the two electrodes (Figure 3.8(a)). When the sample and tip are electrically connected the Fermi levels align and the work function difference leads to an electric field in the barrier region (Figure 3.8(b)). The height of the barrier can roughly be approximated by the average work function of sample and tip. When a voltage is applied across the barrier, electrons on the negative side with an energy

below the Fermi level can tunnel into the empty states on the positive side (Figure 3.8(c)).

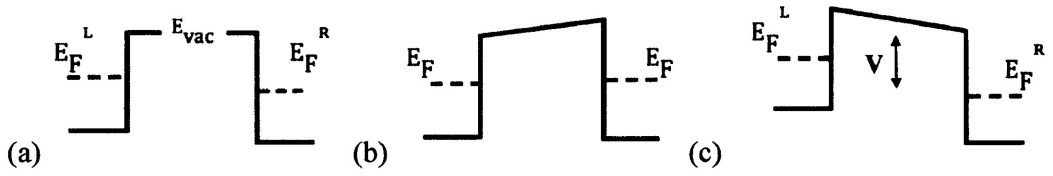

Figure 3.8. A schematic of the potential barrier between probe and surface for vacuum tunneling. (a) When separated the Fermi levels for the two materials differ due to the work function difference. (b) When the two parts are in electrical contact the Fermi levels align. (c) A voltage is applied; the electrons can tunnel in the range of energy indicated by the arrows.

It is known that the tunneling current at small bias and low temperature yields (Wiesendanger 1994):

$$I \propto e^{-2\kappa d} \tag{3-20}$$

Assuming a typical work function value $5eV$ from the equation we find that a change of 1Å in distance between two electrodes reduces the tunneling probability by an order of magnitude. This high sensitivity to seperation makes it possible to measure the tip–sample movement (Z direction) very precisely i.e. at an Ångstrom level. In practical operation a sensitive amplifier, feedback controller and piezoelectrics are used to keep the tunneling current constant as the tip moves along the surface, thus providing a topographical map of the sample surface.

Tersoff and Hamann (1985) developed a theory for tunneling between a surface and a model tip in their 1985 paper. In this paper, they treat the surface 'exactly' and model the tip as a spherical potential well. According to Bardeen (1961), the tunneling current can be expressed as:

$$I = \frac{2\pi e}{\hbar}\sum_{\mu,\nu} f(E_\mu)[1 - f(E_\nu + eV)]\left|M_{\mu\nu}\right|^2 \delta(E_\mu - E_\nu) \tag{3-21}$$

where $f(E)$ is the Fermi function, V is the voltage applied, E_μ and E_v is the energy of state ψ_μ and ψ_ν in the absence of tunneling respectively. $M_{\mu\nu}$ is the tunneling matrix element (Bardeen 1961):

$$M_{\mu\nu} = \frac{\hbar^2}{2m}\int dS \cdot (\psi_\mu^* \nabla\psi_\nu - \psi_\nu \nabla\psi_\mu^*) \qquad (3\text{-}22)$$

where ψ_μ and ψ_ν are single particle wavefunctions with respect to the two electrodes. The integral is over any surface lying entirely within the barrier separating the two sides. Though Equation (3-21) resembles first order perturbation theory, it is different in that ψ_μ and ψ_ν are nonorthogonal and solutions of different Hamiltonians. When the measurements are made at room temperature and at small voltages, we can take the limit of small voltage and temperature and rewrite the Equation (3-21) as:

$$I = \frac{2\pi}{\hbar} e^2 V \sum_{\mu,\nu} |M_{\mu\nu}|^2 \, \delta(E_\mu - E_F)\delta(E_\nu - E_F) \qquad (3\text{-}23)$$

By treating the tip as a point probe the tip wave funcions are arbitrarily localized, then the martix element $M_{\mu\nu}$ is proportional to the amplitude of ψ_ν at position $\overrightarrow{r_0}$ of the tip, so Equation (3-22) can be expressed as:

$$I \propto \sum_\nu |\psi_\nu(\overrightarrow{r_0})|^2 \delta(E_\nu - E_F) \qquad (3\text{-}24)$$

Thus the current is propostional to the local density of states (LODS) of the sample at E_F at the position of the tip. And the STM image is a contour map of constant surface LDOS.

In order to solve Equation (3-23) in general we need to evaluate $M_{\mu\nu}$. Tersoff and Hamann (1985) expanded the surface wavefunction as:

$$\psi_\nu = \Omega_s^{-1/2} \sum_G a_G \exp[(\kappa^2 + |\overrightarrow{\kappa_G}|^2)^{\frac{1}{2}} z] \exp(i\overrightarrow{\kappa_G} \cdot \vec{x}) \qquad (3\text{-}25)$$

Where Ω_s is the sample volume, $\kappa = \hbar^{-1}(2m\phi)^{1/2}$, ϕ is the work function and $\overrightarrow{\kappa_G} = \overrightarrow{k_\parallel} + \vec{G}$, where $\overrightarrow{k_\parallel}$ is the surface Bloch wave vector of the state and $\vec{G}$ is a surface reciprocal-lattice vector. Modeling the tip as a spherical potential well, the wave function of the tip is of the form:

$$\psi_\mu = \Omega_t^{-\frac{1}{2}} c_t \kappa R e^{\kappa R} (\kappa|\vec{r} - \overrightarrow{r_0}|)^{-1} e^{-\kappa|\vec{r} - \overrightarrow{r_0}|} \qquad (3\text{-}26)$$

where Ω_t is the probe volume and κ is the same as in Equation (3-25). Using these wavefunctions Tersoff and Hamann (1985) obtained:

$$M_{\mu\nu} = \frac{\hbar^2}{2m} 4\pi\kappa^{-1}\Omega_t^{-\frac{1}{2}}\kappa R e^{\kappa R}\psi_\nu(\vec{r_0}) \qquad (3\text{-}27)$$

Where κ is the inverse decay length of the wavefunctions in vacuum, $\vec{r_0}$ is the position of the center of curvature of the tip. When substituting Equation (3-27) into Equation (3-23), the tunneling current yields:

$$I = 32\pi^3\hbar^{-1}e^2V\phi^2D_t(E_F)R^2\kappa^{-4}e^{2\kappa R} \times \sum_\nu|\psi_\nu(\vec{r_0})|^2\,\delta(E_\nu - E_F) \qquad (3\text{-}28)$$

Where D_t is the density of states per unit volume of probe tip, ϕ is the work function and E_F is the Fermi level. As before the tunneling current is proportional to the surface LDOS.

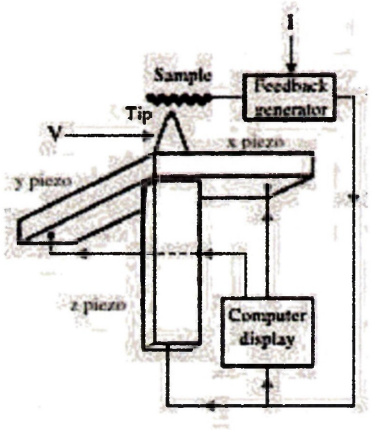

Figure 3.9. A schematic of an STM system. Reproduce from *Modern Techniques of Surface Science – Second Edition* (Woodruff & Delchar 1994)

There are four basic components to a Scanning Tunneling Microscope (see Figure 3.10); the sample, a sharp tip, X-Y-Z scan control and a feedback loop. The tip used in these experiments was an atomically sharp tungsten tip. A good tip is extremely crucial in our experiment since it directly determines the resolution and image quality. An ideal tip should terminate in a single atom. We used an electrochemical etching technique to produce the tip. A tungsten wire is placed into a solution of 1 molar NaOH and a negative potential is applied to a counter electrode. The tungsten wire etches and breaks at the air/solution interface which produces a ragged surface with a high probability of having a single atom at the endpoint. As discussed above, a single atom results in the maximum possible resolution.

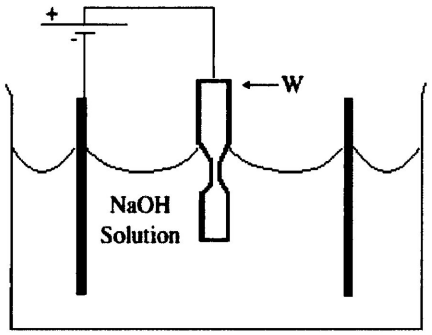

Figure 3.10. A schematic of apparatus for tip preparation.

Once the tip is mounted onto the STM it must be scanned across the surface in an extremely precise manner using a crystal called a piezoelectric which changes its size by very small amounts when an electric field is applied to it. To apply the field the inner and outer surfaces of the piezoelectric tube are covered with metal electrodes. Applying a voltage between the inner and the outer electrode results in elongation/contraction in the Z-direction. The outer electrode is also divided into four sectors to allow deflection in X-Y. Applying a differential voltage between opposite sectors deflects the tube in either X or Y. The piezo sensitivities in X and Y direction for our instrument are 51nm/V and 5nm/V for Z piezo sensitivity.

Our STM uses an inertial system to bring the tip close enough to obtain a tunnel current without crashing the tip. The coarse approach is monitored visually at first and then continued under computer control. One inertial step starts by applying a bias voltage to expand the scan tube fully while checking for a tunneling current. If no current is detected, the scan tube is fully retracted and one coarse step is taken. The inertial system mounts the sample and tip on three orthogonal piezoelectrics to attain coarse motion in X, Y and Z using a "stick-slip" method. In this method a voltage is applied to expend the Z – piezo fully and checking for tunneling current then the voltage is rapidly removed. If no current is detected, the voltage is removed so as to retract the Z – piezo all the way and move the coarse motor. The result of this "slip"

cycle is net motion of the tip in Z or the sample in X or Y. Following the coarse approach step the process is repeated over and over again until a tunneling current is detected. Now we are ready for imaging.

In practical imaging, we measure the topography of the sample surface at constant current. The tunnel current varies exponentially with the gap width so by using a feedback loop the tip is vertically adjusted in such a way that the current always stays constant. Thus the tip will follow the LDOS of the surface at the position of the tip. The STM used in our laboratory is an Omicron Micro SPM and is controlled by RHK Technology[7] SPM 100 electronics.

3.2 Sample preparation

The wafers we use in our experiment are n-type Si(111) miscut by 1° towards $(\overline{1}\overline{1}2)$ purchased from Sil'tronix Silicon[8]. The samples are mounted on a sample holder outside the UHV chamber. Gloves are used to avoid contamination. The wafer is mounted stress free between the two Tantalum coils. The sample holder consists of two metal pieces and was designed so that each side is electrically isolated from the other. The sample was mounted via the two coils bridge the two halves of the holder to permit current to flow through the sample. The current is used to heat the sample. The sample is introduced into the main chamber via the fast entry load lock.

The first step in our experiments is to obtain a Si(111) 7x7 surface. Initially the sample is degased overnight at 690°C. Since the size of each sample is different we must find the heating currents to attain the required temperatures. An Ircon Ultimax Plus UX20P pyrometer[9] with an emissivity setting of 0.6 is used to determine the currents necessary to attain 850, 1060 and 1160°C.

---

[7] RHK Technology. http://www.rhk-tech.com
[8] Sil'tronix Silicon Technologies. http://www.sil-tronix-st.com
[9] Ircon. http://www.ircon.com

To obtain a Si(111) 7x7 surface with an evenly spaced arrays of single steps we use a procedure based on a sequence outlined by Lin et al. (1998). The samples are flashed to 1160°C for *10s* to diffuse residual surface carbon into the bulk. The sample is then cooled to 1060°C within *5s* and held for *1 min,* where single steps are stable. Finally the temperature is quenched to 850°C and held for 1 minute. This quench to 850°C avoids step tripling, and the *1 min* anneal and slow cool down helps develop large 7x7 domains and kink-free step edges. LEED and AES are used to ensure long-range order.

After the Si(111) 7x7 surface is obtained, the second step is silver deposition. Silver films are evaporated from a Tantalum basket. The basket was degased during the baking procedure mentioned previously. The $\sqrt{3}\times\sqrt{3}$ surface can be obtained by depositing 1 ML of Ag and annealing the sample to 600°C. In this case one ML is defined as the areal density of unreconstructed Si atoms in the topmost layer of the (111) face which is 7.8×10^{14} atoms/cm^2. To deposit silver, the evaporator is bought up to the evaporation temperature and preheated for 2 min to allow the flux to stabilize. Then the sample is exposed to the flux for the required time period. Following deposition, the sample is annealed for 2 minutes. LEED and AES are used to check the surface structure and the Ag coverage.

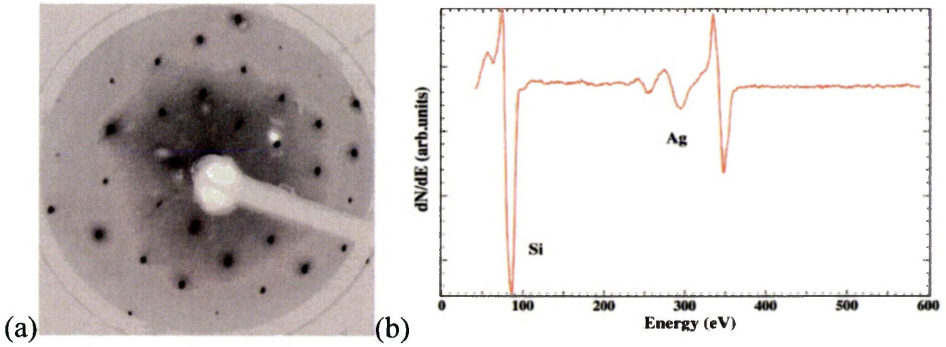

Figure 3.11. (a) A LEED diffraction pattern for the √3 - Ag surface, and (b) the corresponding Auger spectrum showing three Ag MNN transitions.

The last step is molecular deposition. The molecules are placed in an Alumina crucible, which is heated by a tungsten filament. The evaporator we use in our laboratory is an evaporator manufactured by tec tra[10]. Figure 3.12 is a photograph of the molecular evaporator which shows the components.

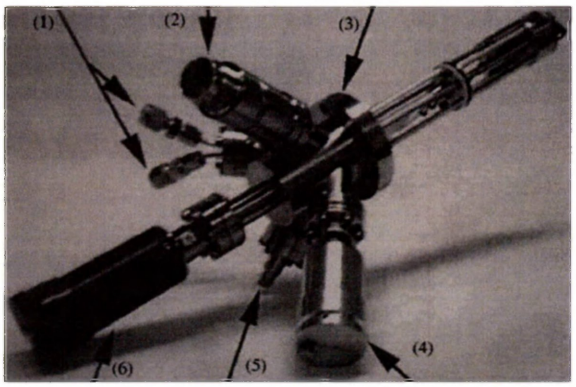

(1) Water Cooling Lines

(2) Power Feedthrough

(3) Mounting Flange

(4) Shutter Control

(5) Flux output

(6) Rod Feed

Figure 3.12. A photograph of the molecular evaporator.

The filament is surrounded by a watercooled copper shroud to shield the chamber from thermal radiation, and to limit the spread of sublimated molecules. A type C thermocouple is connected to monitor the temperature close to the crucible although the true temperature of the crucible is significantly higher.

We use the following sequence to deposit the molecules. The crucible is preheated to a thermocouple reading of 90 °C. At this point the shutter is opened and the sample is exposed to the molecule flux for the duration of the exposure. Following exposure AES is used to determine the molecular coverage.

[10] tec tra. http://www.tectra.de

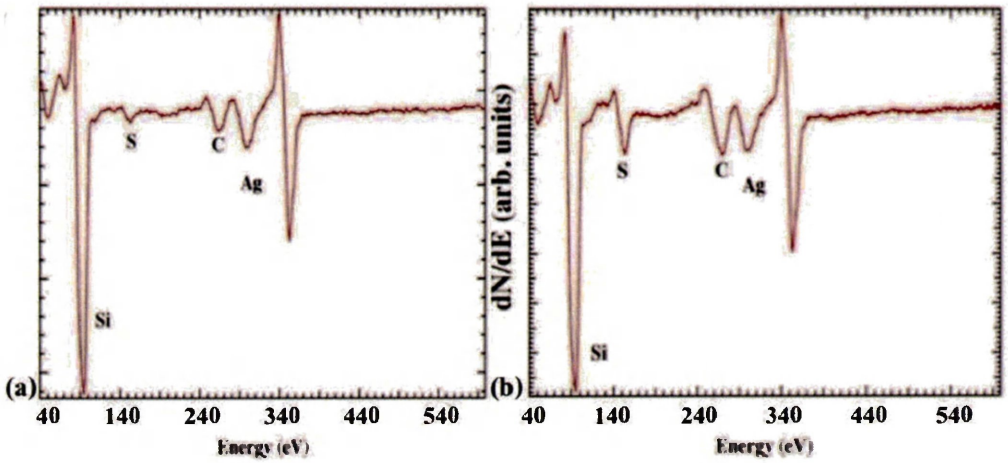

Figure 3.13. Auger spectra after TBTTA deposition for (a) 13 min. and (b) 20 min.

In the case of TBTTA molecules, the AES spectra reveal an Auger LMM transition at 153 eV due to sulfur. Also, due to the existence of carbon in the molecules, we see an increase at 272 eV due to the carbon KLL transition. Unfortunately this is masked by a secondary silver transition (MNN peak) at 351eV. The relative amount of molecules deposited is determined by the change in amplitude of the sulfur peak with respect to the silicon LMM transition at 96 eV. Figure 3.13(a) was obtained following a *13 min.* deposition and the ratio in this instance is S(153 eV)/Si(96 eV) = 0.052. Figure 3.13(b) was obtained following a *20 min* deposition, and the ratio in this instance is 0.143. The bromine peak at 1393 eV was not tracked due to the low signal strength.

CHAPTER 4 Results and Discussion

4.1 Clean √3 - Ag surface

As discussed in the introduction, depositing one monolayer of silver onto the Si(111) 7×7 surface and annealing the resultant surface to 600°C results in a √3×√3 reconstruction. We use both LEED and Auger to verify the formation of the layer. A hexagonal diffraction pattern is observed (see Fig. 4.1(a)), and the Auger spectrum shows a LMM peak for silicon (KE at 96 eV) and three silver LMM peaks (KE at 351eV, 270eV and 220 eV respectively). The ratio of the silver peak to the silicon peak is Ag(351 eV)/Si(96 eV) = 0.59. This ratio is characteristic of one monolayer of silver on the surface.

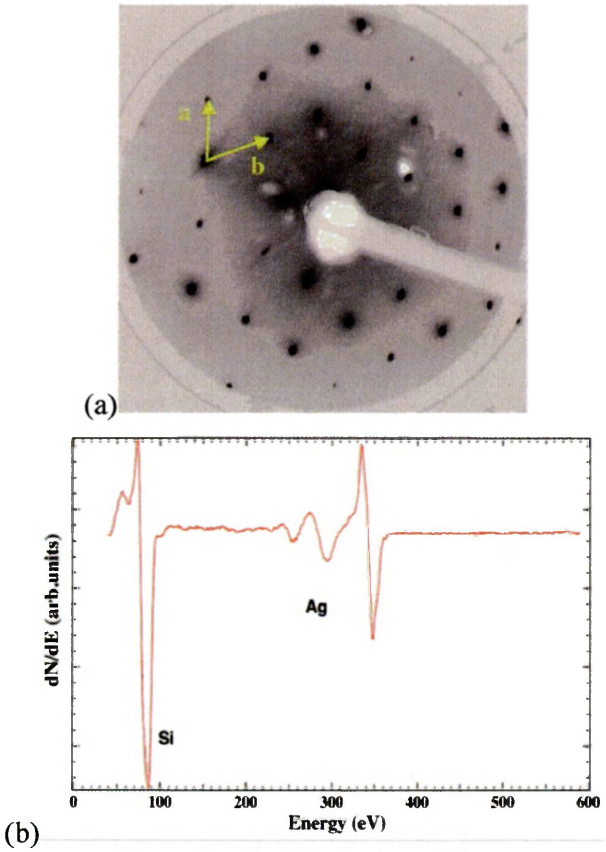

Figure 4.1. (a) LEED diffraction pattern and the reciprocal lattice vectors in yellow lines. The image was obtained at an electron energy of 77 eV. (b) An Auger spectrum for a clean Si(111) - Ag √3×√3 surface. One Si LMM peak and three Ag MNN peaks are observed.

Figure 4.2 shows STM images of the √3 structure. In addition to the periodic structure, the images exhibit several domain boundaries and a number of defects in the √3 structure.

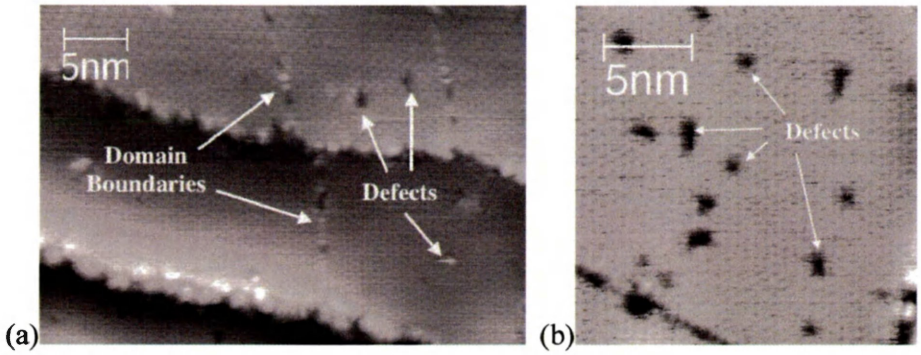

Figure 4.2. STM images of the √3 structure with domain boundaries (a) (U_{bias} = -1.26 V, I_{tunnel} = 0.59 nA 380 Å × 260 Å), and defects (b) (U_{bias} = -1.58V, I_{tunnel} = 0.6 nA 190 Å × 190 Å).

Domain boundaries and defects in the √3-Ag surface reconstruction are inevitable. The domain boundaries arise due to phase mismatch between adjacent √3 domains (Nakayama et al. 1995). These features were observed on all √3 surfaces we prepared, and as we will see play a key role in the structure of the subsequent molecular overlayers.

4.2 Molecular deposition

4.2.1 Coverage Effect

(1) Low Coverage

At very low coverage, no ordered structures of TBTTA were observed. With increasing coverage the molecules initially form 1-d islands. Individual molecules are distinguishable in STM images but the structures are mostly chain-like. (see Figure 4.3)

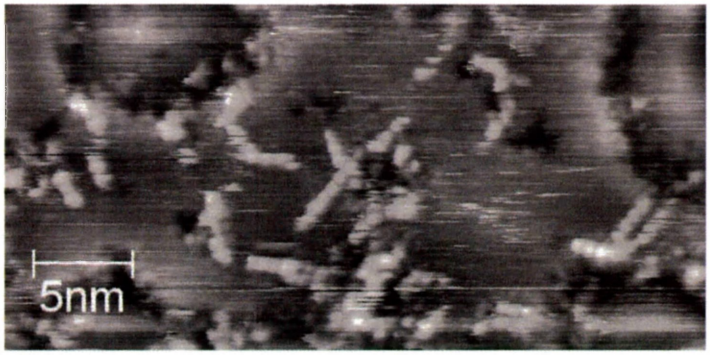

Figure 4.3. An STM image of 1-d TBTTA islands on the √3 surface (U_{bias} = 1.89 V, I_{tunnel} = 257 pA; 350 Å × 170 Å).

Figure 4.4(a) is a representative STM image at somewhat higher TBTTA coverage and the corresponding Auger spectrum. The presence of the sulfur LMM peak at 140 eV associated with TBTTA confirms molecular deposition. We use the ratio of the sulfur to silicon Auger transition as a relative measure of the molecular coverage. According to the Auger data and corresponding STM images, we define 'low coverage' when the ratio of the sulfur LMM peak to the silicon LMM (at a kinetic energy of 96 eV) peak is ~ (0.05 ± 0.01). The actual coverage is likely higher since this estimate ignores mobile TBTTA monomers diffusing on the surface (as discussed below). The STM image in Figure 4.4(a) indicates that molecules do form 2-d supramolecular structures at increased coverage. The ratio of the sulfur LMM peak and the silicon LMM peak in this instance is S(153 eV)/Si(96 eV) = 0.052 (see Figure 4.4 (b)). Under this condition, molecular islands occupy around 20 per cent of the surface.

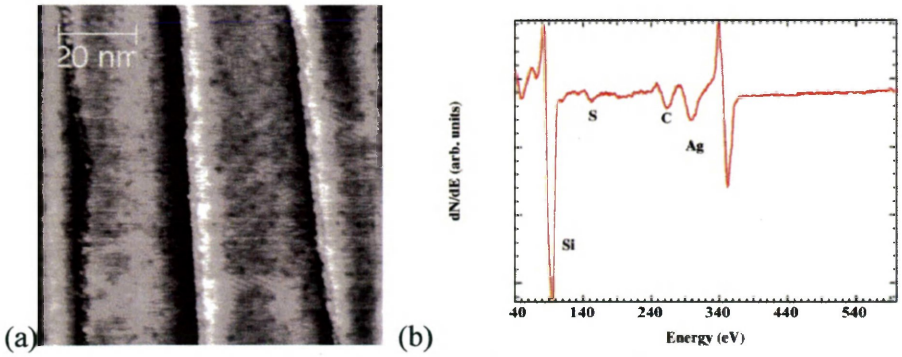

Figure 4.4. (a) STM image with low TBTTA coverage at room temperature (U_{bias} = -1.11 V, I_{tunnel} = 98.4 pA; 880 Å × 880 Å) (b) A corresponding Auger spectrum

In addition to the ordered domains horizontal streaks are evident in the image. This apparent 'noise' is attributed to mobile molecules interacting briefly and randomly with the scanning tip. The diffusing molecules give rise to bright streaks along the fast scan direction (horizontal) of the images. For weakly bound species this 'noise' is often observed in STM images at room temperature. For example, when (Tait et al. 2007) studied the deposition of 1,4-bis(4-pyridyl)benzene on Cu(100) using STM, this 'noise' also appeared in their STM images and they attributed this to extra molecules moving on the surface consistent with our findings. In addition to raster noise, by comparing STM images separated by several minutes, we observe the dissolution and growth of some molecular structures (in Figure 4.5). This is due to the attachment or detachment of monomers from the supramolecular structures and into or out of the 2-d molecular gas on the surface. This dynamic behavior indicates relatively weak molecule-molecule interactions, and high mobility for TBTTA monomers on the √3-Ag surface.

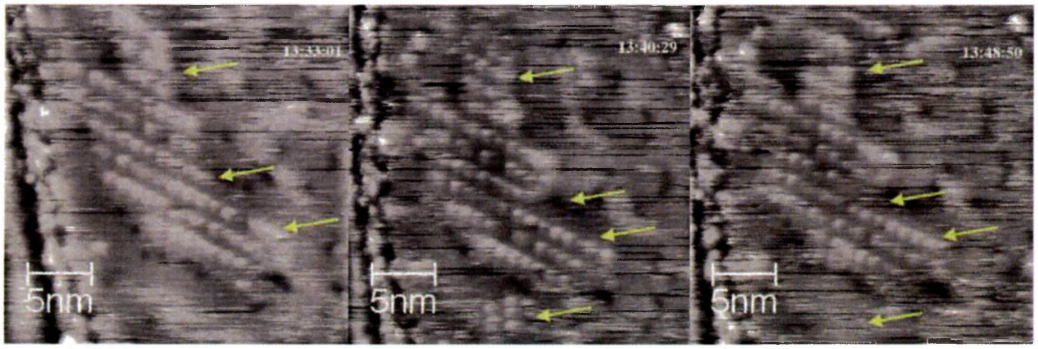

Figure 4.5. Consecutive STM images in the same region, time obtained marked at top right. Yellow arrows indicate changes (U_{bias} = -1.0 V, I_{tunnel} = 97.7 pA; 260 Å × 260 Å).

We also found that these supramolecular structures are quite sensitive to changes in the STM bias conditions. Though specific values vary depending on the tip condition, we observed that the structures decomposed when imaging at high bias ($> |2| V$) or at low bias ($< |0.7| V$). At high bias we believe the increased electric field is breaking

the structures apart, whereas at low bias molecules are swept away due to the physical contact with the tip.

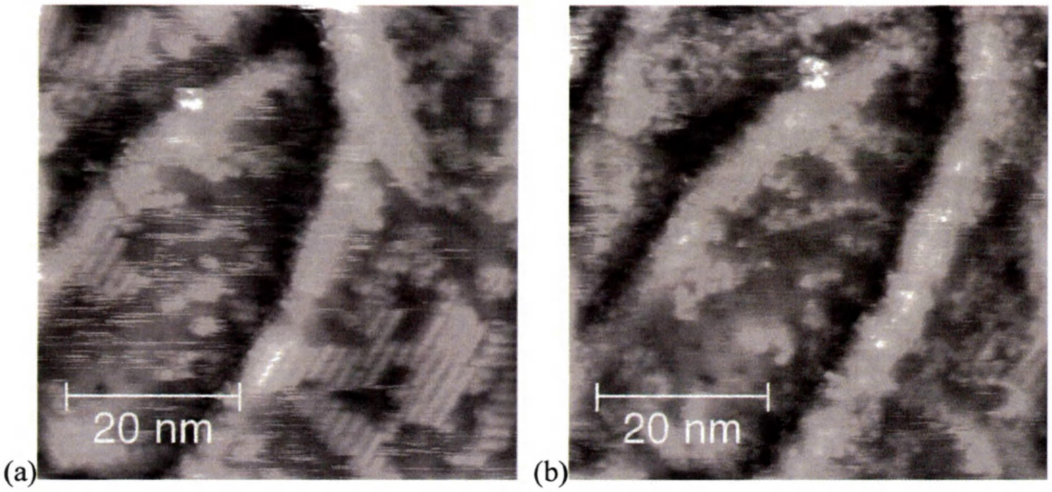

Figure 4.6. Two STM images taken at the same spot. (a) shows a surface initially with molecular islands, (b) which are completely decomposed after several scanning.
(U_{bias} = 1.61 V, I_{tunnel} = 110 pA, 550 Å×550 Å)

(2) Unit Cell

In Figure 4.7, the high resolution STM image shows that supramolecular structures are in three orientational domains with an angle of 120° between them. This is consistent with the 3-fold symmetry of the underlying structure $\sqrt{3}$ lattice.

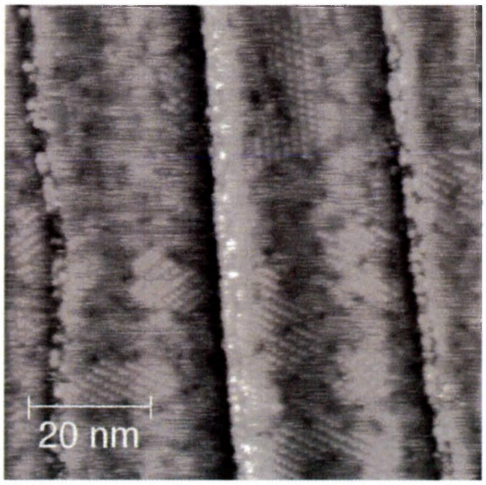

Figure 4.7. An STM image with low coverage of TBTTA (U_{bias} = -1.2 V, I_{tunnel} = 109 pA, 770 Å×770 Å)

At low coverage, only one molecular arrangement (type I) is observed. In the high-resolution STM images such as Figure 4.8(a), the type I structure can be distinguished. The bright features in the image arrange to form an oblique unit cell (see Figure 4.8(b)) with lattice parameters $\boldsymbol{a}$ = (10 ± 1) Å, $\boldsymbol{b}$ = (15 ± 1) Å with an internal angle of $\boldsymbol{\alpha}$ = (70 ± 2)°. The error bars are based on the variation between measurements made on a number of different images.

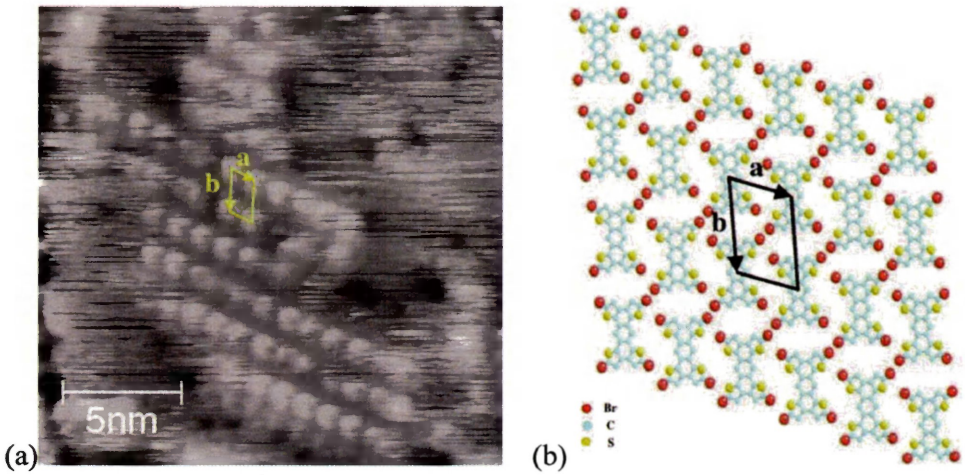

Figure 4.8. (a) molecular detail of a type I domain (U_{bias} = -1.0 V, I_{tunnel} = 90 pA; 190 Å × 190 Å). (b) A Proposed molecular structure for type I supramolecular unit cell.

It is intriguing that the molecular arrangement of the type I structure is very similar to that observed by Gutzler et al. who deposited TBTTA monomers onto highly oriented pyrolytic graphite (HOPG). The surface of HOPG is quite unreactive. To understand the observed unit cell on HOPG, Gutzler et al. (2012) performed density functional theory (DFT) calculations. Neglecting molecule-surface interactions entirely they considered a number of intermolecular interactions and the resultant molecular structure they determined is show in Figure 4.9.

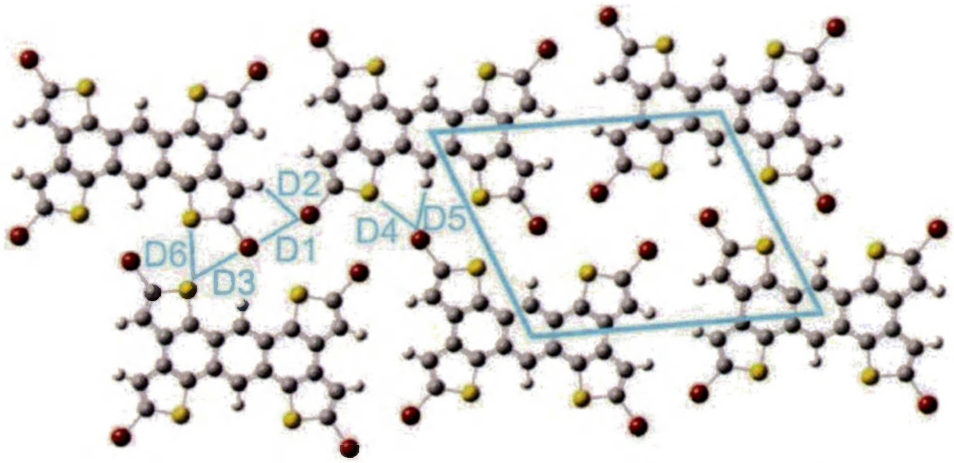

Figure 4.9. Calculated unit cell of TBTTA on HOPG. Graph from (Gutzler et al. 2012)

To determine the structure they considered a number of intermolecular interactions including the Br-Br interaction, *D1; D2* the Br-H interaction; and *D4* the Br-S interaction. They considered a number of configurations and the one shown in Figure 4.9 was of the lowest energy.

The fact that the lowest energy configuration on HOPG is almost identical to the cell we observe on the $\sqrt{3}$ surface indicates that similar intermolecular interactions are the driving force for the arrangement of the TBTTA molecules on our surface.

(3) Molecular Epitaxy

Figure 4.10 is a smaller scale image at a low coverage of TBTTA. The characteristic hexagonal reconstruction of Ag-$\sqrt{3}\times\sqrt{3}$ is visible in addition to a molecular island. STM images that include both the molecular structures and the $\sqrt{3}$ lattice allow us determine the precise relationship between the two. Using this image and others like it we determined that one axis of the molecular unit cell (line b) is rotated by approximately $(45 \pm 5)°$ with respect to a principal $\sqrt{3}$-Ag direction (line c).

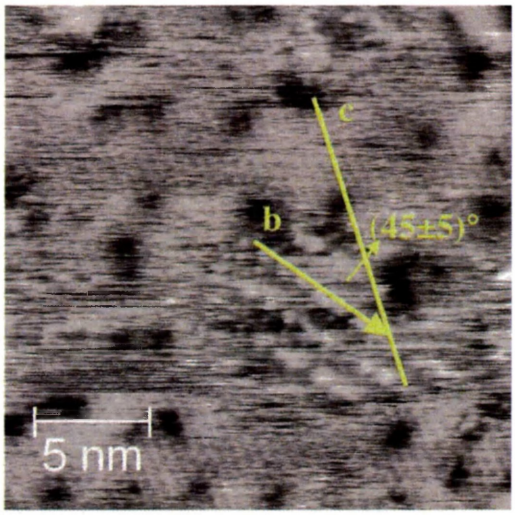

Figure 4.10. A STM image of molecular structure with √3 structure. (U_{bias} = -1.0V, I_{tunnel} = 90.4 pA; 215 Å × 215 Å)

Using the data above, we can express the relationship between the overlayer lattice vector ***a***, ***b*** and √3 lattice vectors ***a'*** and ***b'*** (each with a magnitude of 6.7 Å) in matrix form as:

$$\begin{pmatrix} a \\ b \end{pmatrix} = \begin{pmatrix} 1.0 & 2.0 \\ 2.6 & 0.85 \end{pmatrix} \begin{pmatrix} a' \\ b' \end{pmatrix} \qquad (4\text{-}1)$$

Figure 4.11 is a schematic of proposed unit cell for type I with respect to the √3 lattice according to the parameters we measured in the STM images. As with our previous measurements these numbers are accurate to within 10 per cent. These results (Figure 4.11) suggest that the overlayer is incommensurate with respect to the √3 lattice of the substrate.

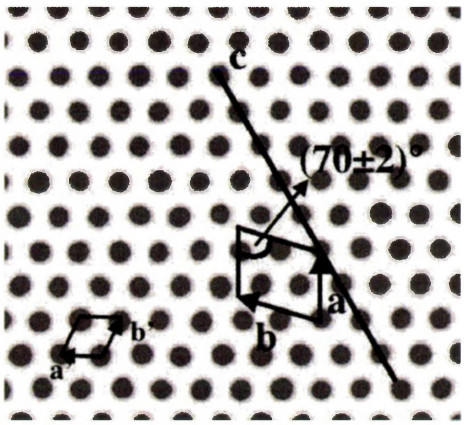

Figure 4.11. Proposed lattice structure from experimental measurement.

Taking measurement error into account, we think it is also necessary to consider the closest commensurate structure to our measurement. The most likely commensurate supramolecular unit cell can be expressed as:

$$\begin{pmatrix} a \\ b \end{pmatrix} = \begin{pmatrix} 1 & 2 \\ 3 & 1 \end{pmatrix} \begin{pmatrix} a' \\ b' \end{pmatrix} \quad (4\text{-}2)$$

Where $\boldsymbol{a}$ = 11.6 Å, $\boldsymbol{b}$ = 17.7 Å is comparable to our experimental result both numerically and structurally. (see Figure 4.12)

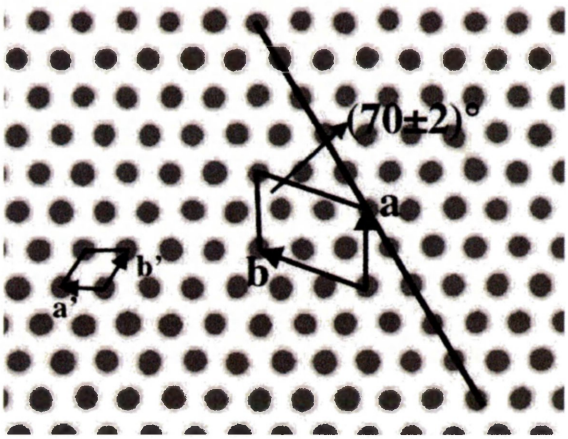

Figure 4.12. A proposed unit cell for type I with respect to the √3 lattice under assumption that the lattice vector is of commensurate with the √3 structure.

In summary, we find that the inter-molecular interactions of TBTTA molecules on √3-Ag are weak. The molecular structures are held together by van der Waals force between monomers and can easily decompose even during the scanning process due to the effect of bias. Other than determining the orientation of the molecular domains the substrate plays a minor role in the formation of the type I structures.

(4) High Coverage

Figure 4.13 is an example of an STM image at higher TBTTA coverage and the corresponding AES. The AES ratio is 0.143 in this instance. The image indicates that molecular islands occupy more than 80 per cent of the surface. Again, actual coverage is likely higher due to the mobile TBTTA monomers moving on the surface. With

increasing molecular coverage the extant and stability of the molecular structures increases.

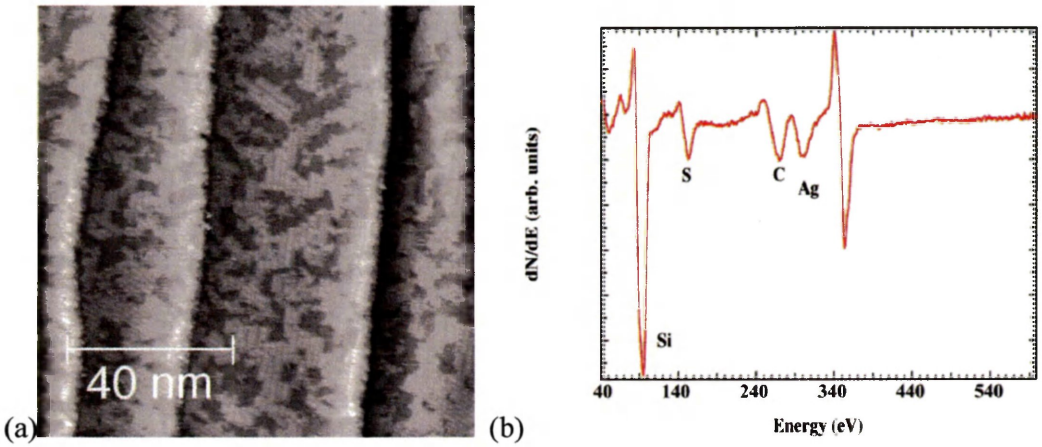

Figure 4.13. (a) An STM image at TBTTA higher coverage (U_{bias} = -1.2V, I_{tunnel} = 483 pA 1040 Å × 1040 Å), and the (b) A corresponding Auger spectrum.

At high coverage, we often find two periodic arrangements on the surface; the 2-d arrangement previously discussed (indicated by the arrow in Figure 4.14) (type I), and a 1-d chain like arrangement (circled in Figure 4.14) (type II). The type II arrangement usually occurs at the edge of a type I structure. Figure 4.15 shows a detailed view of a type II region. The structure is a 1-d chain like structure, with a periodicity along the chain of (9.5 ± 0.5) Å.

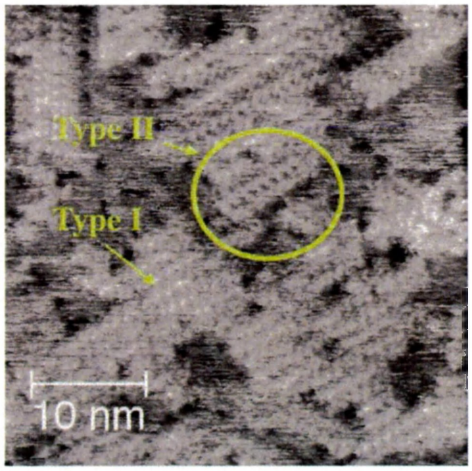

Figure 4.14. An STM image with type I and type II structures evident as highlighted (U_{bias} = -1.0 V, I_{tunnel} = 476 pA; 400 Å × 400 Å).

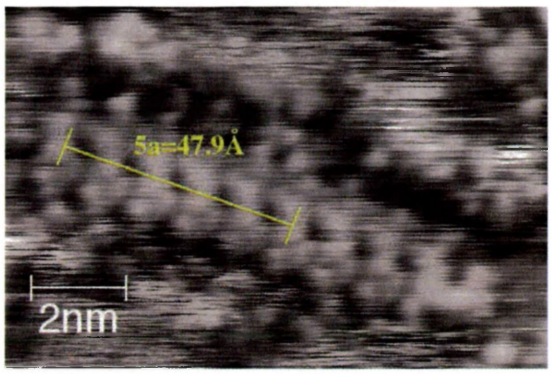

Figure 4.15. STM image of type II structure (U_{bias} = -1.24 V, I_{tunnel} = 454 pA; 110 Å × 75 Å).

Although the origin of this type II structure is uncertain, a number of possibilities can be considered. For example, the formation could be due to dehalogenation followed by the recombination of the molecules. Previous results however have shown that dehalogenation of TBTTA does not occur at room temperature and requires annealing (Gutzler et al. 2014).

4.2.2 Effect of Defects and Domain Boundaries in the √3 Layer

In the STM image in Figure 4.16, we see several supramolecular islands and the bare √3-Ag surface (darker portions). Yellow arrows in the figure point to defects and domain boundaries on √3 structure. It is apparent that the supramolecular structures terminate or avoid these defects and domain boundaries in the √3 surface. As discussed, domain boundaries and defects on √3 structure are inevitable. Our results suggest that these aperiodic features can limit the extent of the supramolecular domains. At domain boundaries and defects there is a loss of periodicity and as a result they limit the periodic molecular structures

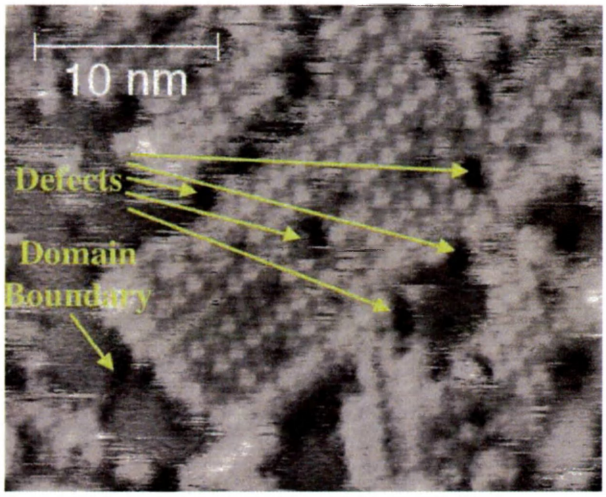

Figure 4.16. An STM image of supramolecular structures on the √3 surface. The extent of the structures appears to be limited by defects and a domain boundaries on √3 structure. (U_{bias} = -1.11 V, I_{tunnel} = 497 pA; 320 Å × 270 Å).

4.2.3 Annealing Studies

As stated, the type I structures are weakly held together. In an effort to produce more robust structures we have annealed the samples. Gutzler et al. (2014) found that annealing at 400°C on single crystal Ag surfaces allowed TBTTA molecules to dehalogenate and form covalent structures. The annealing step was required to cleave the Br-C bonds and allow the covalent C-C bonds to form between monomers.

We made several attempts to anneal the samples to temperatures, ranging from 145°C to 400°C. At temperatures higher than 400°C Auger spectroscopy indicates that the √3 structure is modified. Spectra reveal that the amplitude of the Ag peaks are reduced (see Figure 4.17) and the S LMM (140 eV) peak is somewhat reduced indicating changes to the molecules.

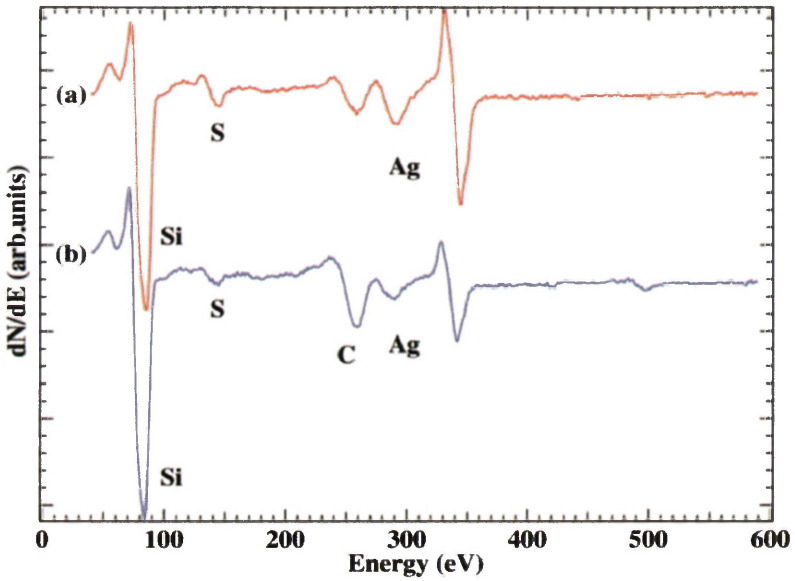

Figure 4.17. An Auger spectrum before (trace a) and after annealing the sample at 425°C (trace b). The peak at 500 eV is due to oxygen may be due to the fact that the sample has been in the chamber for an extended period.

STM images also provide evidence that this temperature is too high. No supramolecular structures are seen but 3-d islands are observed on the surface. The 3-d islands were not observed prior to annealing and could be due to Ag or C agglomeration as a result of molecular decomposition. Moreover, at this temperature, the $\sqrt{3}$ structure on the surface appears to have been destroyed (See Figure 4.18 (a)).

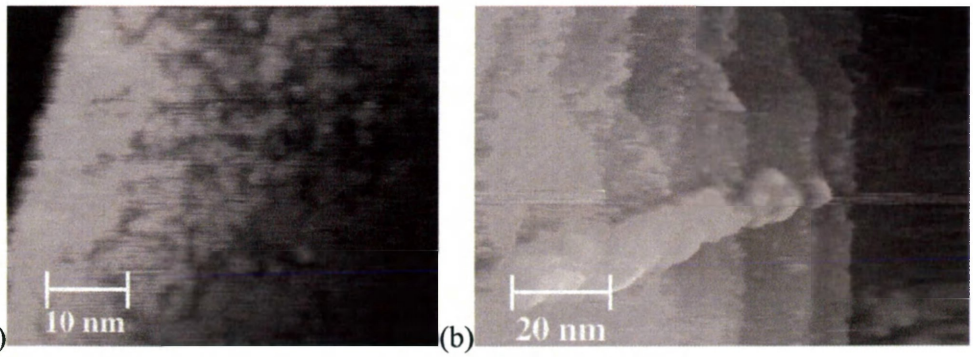

Figure 4.18. (a) A Broken Ag substrate structure after annealing the sample at 425°C (b) recrystallized structure of silver (U_{bias} = 1.21 V, I_{tunnel} = 0.5 nA; 510 Å × 410 Å)

After annealing room temperature deposited samples at 280°C, we measured a small change in the Ag LMM peak, a slight decrease in the sulfur peak; a large increase in the carbon peak and the appearance of a very small oxygen peak at 500 eV. The

oxygen could be due to the fact that the sample had been in the chamber for considerable period of time. (see Figure 4.19).

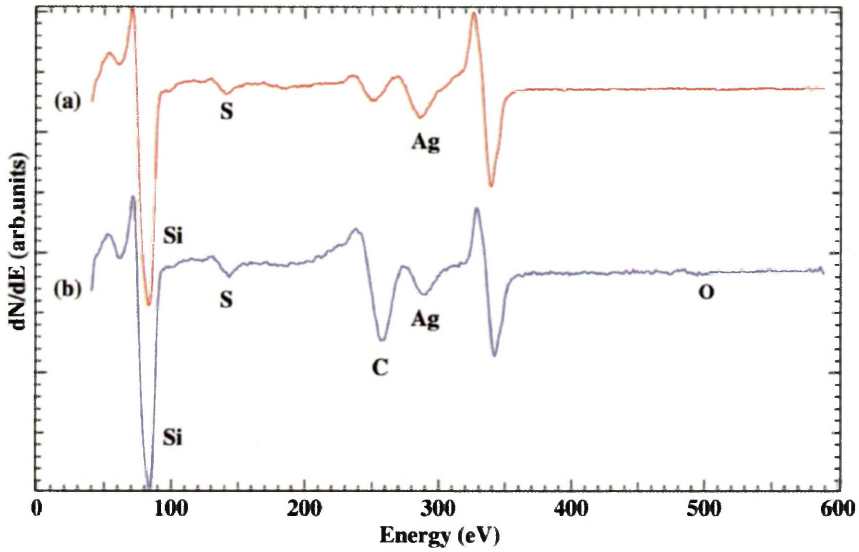

Figure 4.19. An Auger spectrum before (trace a) and after annealing the sample at 280°C (trace b).

STM images obtained following annealing at 280 °C show that the $\sqrt{3}$ structure is intact. In Figure 4.20 no ordered molecular structures are observed and rather we see disordered features distributed uniformly about the surface. Combined with the Auger results we conclude that the molecules have decomposed. Similar results are observed following annealing at temperatures between 160°C ~ 280°C.

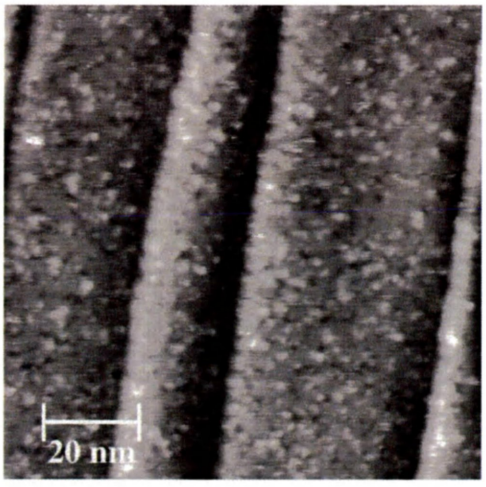

Figure 4.20. Molecular features are distributed uniformly on the surface (U_{bias} = 1.2 V, I_{tunnel} = 0.53 nA; 960 Å × 960 Å) after annealing at 280°C.

At 145°C Auger data does not indicate any stoichiometric changes after annealing (see Figure 4.21). The Auger ratio in red is S(140 eV)/Si(96 eV) = 0.10 and corresponds to a low molecular coverage i.e. less than the molecular coverage shown in Figure 4.7.

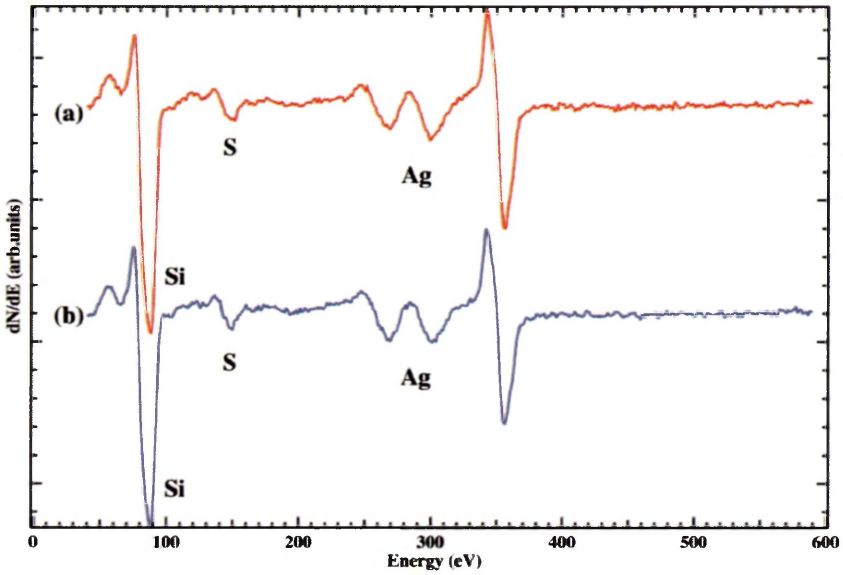

Figure 4.21. An Auger spectrum before (trace a) and after annealing the sample at 145°C (trace b).

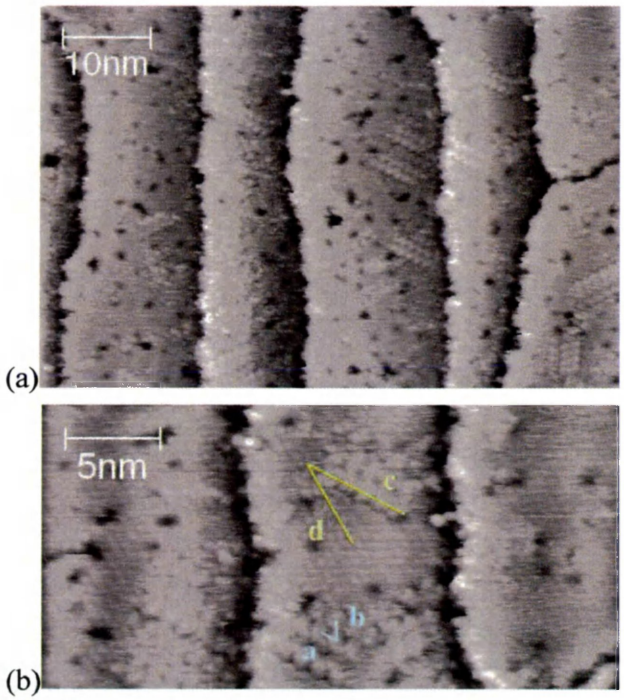

Figure 4.22. (a) An STM image of ordered structures after annealing at 145°C (U_{bias} = 1.2 V, I_{tunnel} = 320 pA; 640 Å × 420 Å). (b) ***a*** is along the direction of the molecular chains, ***b*** is along the one of the

principal directions of √3 structure (U_{bias} = 1.2 V, I_{tunnel} = 306 pA; 300 Å × 150 Å).

The high-resolution STM images obtained on this sample exhibit ordered structures (Figure 4.22 (a)). The ordered structures are unlike those observed at room temperature. The structures occur predominately as two rows and with another extra row in some instances. The periodicity along the chains measures (10 ± 0.5) Å (line *a* in Figure 4.22 (b)) and the distance between similar features in adjacent chains is also (10 ± 0.5) Å (line b). The chain direction is rotated by (30 ± 2)° with respect to the √3 direction (line d). With these data, we can express the structure in matrix form as:

$$\begin{pmatrix} a \\ b \end{pmatrix} = \begin{pmatrix} 1 & 2 \\ 2 & 1 \end{pmatrix} \begin{pmatrix} a' \\ b' \end{pmatrix} \tag{4-3}$$

Figure 4.23 shows the corresponding schematic of the proposed epitaxial relationship for the 'two row' structure:

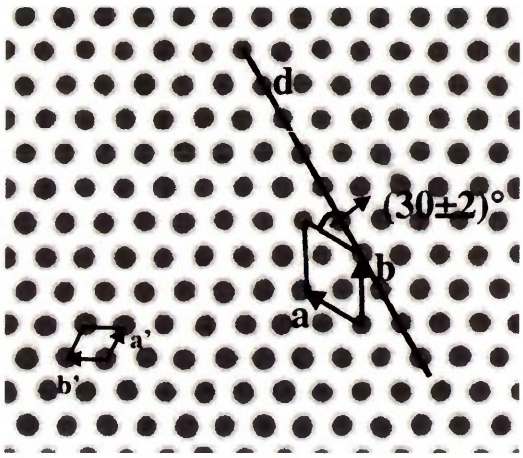

Figure 4.23. A schematic of lattice structure for molecules after annealing.

The 10 Å spacing between features is smaller than the supramolecular structures observed at room temperature. Moreover, in contrast to the type I structures at room temperature, these structures exhibit increased stability under repeated scanning under bias conditions ranging from – 1.2 V to + 1.2 V. All characteristics above indicate a dehalogenation reaction may have occurred at the surface and the ordered structure could be monomers bonded to one another in a covalent network. Another possibility is the structure is an assembly of bromine atoms following dehalogenation. According

to Gutzler et al. (2014), when bromine atoms are cleaved from TBTTA on noble metal surfaces during the dehalogenation reaction, they tend to form small circular protrusions surrounding the molecules, however this has not been observed on our surface. The nature of these structures is unclear at this time and more work with samples at higher coverage will be required to determine the properties. In addition theoretical calculations may shed light on the barrier to dehalogenation on the $\sqrt{3}$ surface.

CHAPTER 5 Summary

I have described experiments depositing TBTTA molecules onto the Si(111) $\sqrt{3}\times\sqrt{3}$-Ag surface. Evidence from STM images indicates that TBTTA molecules deposited at room temperature are quite mobile and readily form 2-d ordered structures on the $\sqrt{3}$-Ag surface at low coverage. The molecules initially form 2-d dendritic islands and eventually form compact supramolecular structures. We found the molecular structures in three orientational domains consistent with the threefold symmetry of the substrate surface. The supramolecular structure has an oblique 2-d unit cell with lattice parameters $\boldsymbol{a}$ = (10 ± 1) Å, $\boldsymbol{b}$ = (15 ± 1) Å and an internal angle of $\boldsymbol{\alpha}$ = (70 ± 2)°. We found that one axis (along $\boldsymbol{b}$) of the molecular unit cell is rotated by approximately (45 ± 5)° with respect to a principal $\sqrt{3}$-Ag direction. The relationship between the overlayer and $\sqrt{3}$ lattice in matrix form is:

$$\begin{pmatrix} a \\ b \end{pmatrix} = \begin{pmatrix} 1.0 & 2.0 \\ 2.6 & 0.85 \end{pmatrix} \begin{pmatrix} a' \\ b' \end{pmatrix} \tag{5-1}$$

This matrix indicates that the predominant structure is incommensurate with the $\sqrt{3}$ structure based on our measurements. This structure is similar to the unit cell observed on HOPG which DFT calculations indicate is determined primarily by van der Waals interactions between molecules (Gutzler et al. 2012). If the overlayer structure is commensurate with the $\sqrt{3}$ substrate, the closest possible structure would be:

$$\begin{pmatrix} a \\ b \end{pmatrix} = \begin{pmatrix} 1 & 2 \\ 3 & 1 \end{pmatrix} \begin{pmatrix} a' \\ b' \end{pmatrix} \tag{5-2}$$

The extent of these type I structures is often limited by defects and domain boundaries in the underlying $\sqrt{3}$-Ag structure. We also found that this structure is quite fragile and can decompose under STM imaging at both high bias ($> |2|\ V$) and low bias conditions ($< |0.7|\ V$).

With increasing coverage, the molecular structures form more compact structures that exhibit higher stability at room temperature. At high coverage, in addition to the supramolecular domains outlined above, we also observe 1-d structures with a

periodicity along the structure of (9 ± 0.5) Å. These type II structures primarily occur at edge of the type I structure. The origin of these structures is still uncertain and further investigation is required.

We have also investigated the effect of annealing on the room temperature TBTTA structures. Temperatures higher than 400°C result in damage to the underlying $\sqrt{3}$-Ag structure. At temperatures between 160°C ~ 280°C, the $\sqrt{3}$ surface remains intact however the molecules decompose. Preliminary results at 145°C are promising. We have observed ordered structures on surface. The structures appear to contain two parallel chains, with a third row in some cases. The periodicity along the chains measures (10 ± 0.5) Å and the distance between similar features in adjacent chains is also (10 ± 0.5) Å. The chain direction is rotated by (30 ± 2)° with respect to the $\sqrt{3}$ direction. Repeated scanning under different bias conditions indicates these structures exhibit increased stability compared to the room temperature structures. These initial results indicate that thermal energy can lead to a structural rearrangement of TBTTA molecules on the surface. More experiments and theoretical calculations are needed to shed some light in the future works.

REFERENCES

Bardeen, J. (1961). Tunnelling from a many-particle point of view. *Physical Review Letters*, 6: 57-59.

Bartels, L. (2010). Tailoring molecular layers at metal surfaces. *Nature Chemistry*, 2 (2): 87-95.

Bieri, M., Nguyen, M. T., Groning, O., Cai, J. M., Treier, M., Ait-Mansour, K., Ruffieux, P., Pignedoli, C. A., Passerone, D., Kastler, M., et al. (2010). Two-Dimensional Polymer Formation on Surfaces: Insight into the Roles of Precursor Mobility and Reactivity. *Journal of the American Chemical Society*, 132 (46): 16669-16676.

Binnig, G. & Rohrer, H. (1986). Scanning tunneling microscopy. *IBM Journal of Research and Development 30: 4*.

Brown, D. E., Moffatt, D. J. & Wolkow, R. A. (1998). Isolation of an intrinsic precursor to molecular chemisorption. *Science*, 279 (5350): 542-544.

Brusso, J. L., Hirst, O. D., Dadvand, A., Ganesan, S., Cicoira, F., Robertson, C. M., Oakley, R. T., Rosei, F. & Perepichkat, D. F. (2008). Two-dimensional structural motif in thienoacene semiconductors: Synthesis, structure, and properties of tetrathienoanthracene isomers. *Chemistry of Materials*, 20 (7): 2484-2494.

Cai, J. M., Ruffieux, P., Jaafar, R., Bieri, M., Braun, T., Blankenburg, S., Muoth, M., Seitsonen, A. P., Saleh, M., Feng, X. L., et al. (2010). Atomically precise bottom-up fabrication of graphene nanoribbons. *Nature*, 466 (7305): 470-473.

Carbone, M., Piancastelli, M. N., Zanoni, R., Comtet, G., Dujardin, G. & Hellner, L. (1998). A low symmetry adsorption state of benzene on Si(111)7x7 studied by photoemission and photodesorption. *Surface Science*, 407 (1-3): 275-281.

Champness, N. R. (2007). Building with molecules. *Nature Nanotechnology*, 2 (11): 671-672.

Chung, K. H., Park, J., Kim, K. Y., Yoon, J. K., Kim, H., Han, S. & Kahng, S. J. (2011). Polymorphic porous supramolecular networks mediated by halogen bonds on Ag(111). *Chemical Communications*, 47 (41): 11492-11494.

Clarke, S. M., Friscic, T., Jones, W., Mandal, A., Sun, C. G. & Parker, J. E. (2011). Observation of a two-dimensional halogen-bonded cocrystal at sub-monolayer coverage using synchrotron X-ray diffraction. *Chemical Communications*, 47 (9): 2526-2528.

El Garah, M., MacLeod, J. M. & Rosei, F. (2013). Covalently bonded networks through surface-confined polymerization. *Surface Science*, 613: 6-14.

Franc, G. & Gourdon, A. (2011). Covalent networks through on-surface chemistry in ultra-high vacuum: state-of-the-art and recent developments. *Physical Chemistry Chemical Physics*, 13 (32): 14283-14292.

Giessibl, F. J., Bielefeldt, H., Hembacher, S. & Mannhart, J. (2001). Imaging of atomic orbitals with the Atomic Force Microscope - experiments and simulations. *Annalen Der Physik*, 10 (11-12): 887-910.

Gourdon, A. (2008). On-surface covalent coupling in ultrahigh vacuum. *Angewandte Chemie-International Edition*, 47 (37): 6950-6953.

Grill, L., Dyer, M., Lafferentz, L., Persson, M., Peters, M. V. & Hecht, S. (2007). Nano-architectures by covalent assembly of molecular building blocks. *Nature Nanotechnology*, 2 (11): 687-691.

Gutzler, R., Fu, C. Y., Dadvand, A., Hua, Y., MacLeod, J. M., Rosei, F. & Perepichka, D. F. (2012). Halogen bonds in 2D supramolecular self-assembly of organic semiconductors. *Nanoscale*, 4 (19): 5965-5971.

Gutzler, R., Cardenas, L., Lipton-Duffin, J., El Garah, M., Dinca, L. E., Szakacs, C. E., Fu, C. Y., Gallagher,

M., Vondracek, M., Rybachuk, M., et al. (2014). Ullmann-type coupling of brominated tetrathienoanthracene on copper and silver. *Nanoscale*, 6 (5): 2660-2668.

Hedberg, C. L. (1995). *Handbook of Auger Electron Spectroscopy*. Third ed. Minnesota: Physical Electronics, Inc.

Hooks, D. E., Fritz, T. & Ward, M. D. (2001). Epitaxy and molecular organization on solid substrates. *Advanced Materials*, 13 (4): 227-+.

Kowarik, S., Gerlach, A. & Schreiber, F. (2008). Organic molecular beam deposition: fundamentals, growth dynamics, and in situ studies. *Journal of Physics-Condensed Matter*, 20 (18).

Lackinger, M. & Heckl, W. M. (2011). A STM perspective on covalent intermolecular coupling reactions on surfaces. *Journal of Physics D-Applied Physics*, 44 (46).

Landauer, G. (1962). Generation of harmonics of the electron-gyrofrequency in a penning discharge. *J. Nucl. Energy, Part C Plasma Phys*, 4: 395.

Lin, J. L., Petrovykh, D. Y., Viernow, J., Men, F. K., Seo, D. J. & Himpsel, F. J. (1998). Formation of regular step arrays on Si(111)7x7. *Journal of Applied Physics*, 84 (1): 255-260.

McCullough, R. D. (1998). The chemistry of conducting polythiophenes. *Advanced Materials*, 10 (2): 93-+.

Murphy, B. E., Krasnikov, S. A., Cafolla, A. A., Sergeeva, N. N., Vinogradov, N. A., Beggan, J. P., Lubben, O., Senge, M. O. & Shvets, I. V. (2012). Growth and ordering of Ni(II) diphenylporphyrin monolayers on Ag(111) and Ag/Si(111) studied by STM and LEED. *Journal of Physics-Condensed Matter*, 24 (4).

Nakayama, T., Watanabe, S. & Aono, M. (1995). Structure and stability of the out-of-phase boundary in a surface superlattice, Si(111)root 3x root 3R30 degrees-Ag. *Surface Science*, 344 (1-2): 143-148.

Palma, C. A. & Samori, P. (2011). Blueprinting macromolecular electronics. *Nature Chemistry*, 3 (6): 431-436.

Perepichka, D. F. & Rosei, F. (2009). CHEMISTRY Extending Polymer Conjugation into the Second Dimension. *Science*, 323 (5911): 216-217.

Schlogl, S., Sirtl, T., Eichhorn, J., Heckl, W. M. & Lackinger, M. (2011). Synthesis of two-dimensional phenylene-boroxine networks through in vacuo condensation and on-surface radical addition. *Chemical Communications*, 47 (45): 12355-12357.

Suzuki, T., Lutz, T., Payer, D., Lin, N., Tait, S. L., Costantini, G. & Kern, K. (2009). Substrate effect on supramolecular self-assembly: from semiconductors to metals. *Physical Chemistry Chemical Physics*, 11 (30): 6498-6504.

Tait, S. L., Langner, A., Lin, N., Stepanow, S., Rajadurai, C., Ruben, M. & Kern, K. (2007). One-dimensional self-assembled molecular chains on Cu(100): Interplay between surface-assisted coordination chemistry and substrate commensurability. *Journal of Physical Chemistry C*, 111 (29): 10982-10987.

Takahashi, T., Nakatani, S., Okamoto, N., Ishikawa, T. & Kikuta, S. (1988). STUDY ON THE SI(111) SQUARE-ROOT-3 X SQUARE-ROOT-3-AG SURFACE-STRUCTURE BY X-RAY-DIFFRACTION. *Japanese Journal of Applied Physics Part 2-Letters*, 27 (5): L753-L755.

Takahashi, T., Nakatani, S., Okamoto, N., Ishikawa, T. & Kikuta, S. (1991). A STUDY OF THE SI(111)-SQUARE-ROOT-3X-SQUARE-ROOT-3-AG SURFACE BY TRANSMISSION-X-RAY DIFFRACTION AND X-RAY-DIFFRACTION TOPOGRAPHY. *Surface Science*, 242 (1-3): 54-58.

Takahashi, T. & Nakatani, S. (1993). REFINEMENT OF THE SI(111)ROOT-3X-ROOT-3-AG STRUCTURE BY

SURFACE X-RAY-DIFFRACTION. *Surface Science*, 282 (1-2): 17-32.

Takayanagi, K., Tanishiro, Y., Takahashi, S. & Takahashi, M. (1985). STRUCTURE-ANALYSIS OF SI(111)-7X7 RECONSTRUCTED SURFACE BY TRANSMISSION ELECTRON-DIFFRACTION. *Surface Science*, 164 (2-3): 367-392.

Takimiya, K., Ebata, H., Sakamoto, K., Izawa, T., Otsubo, T. & Kunugi, Y. (2006). 2,7-Diphenyl 1 benzothieno 3,2-b benzothiophene, a new organic semiconductor for air-stable organic field-effect transistors with mobilities up to 2.0 cm(2) V-1 s(-1). *Journal of the American Chemical Society*, 128 (39): 12604-12605.

Tersoff, J. & Hamann, D. R. (1985). THEORY OF THE SCANNING TUNNELING MICROSCOPE. *Physical Review B*, 31 (2): 805-813.

Tong, X., Ohuchi, S., Tanikawa, T., Harasawa, A., Okuda, T., Aoyagi, Y., Kinoshita, T. & Hasegawa, S. (2002). Core-level photoemission of the Si(111)-root 21 x root 21-Ag surface using synchrotron radiation. *Applied Surface Science*, 190 (1-4): 121-128.

Umbach, E., Sokolowski, M. & Fink, R. (1996). Substrate-interaction, long-range order, and epitaxy of large organic adsorbates. *Applied Physics a-Materials Science & Processing*, 63 (6): 565-576.

VanHove, M. A., Weinberg, W. H. & Chan, C. M. (1986). *Low-Energy Electron Diffraction: Experiment, Theory and Surface Structure Determination*. Springer Series in Surface Sciences, vol. 6. Berlin: Springer Verlag.

Walch, H., Gutzler, R., Sirtl, T., Eder, G. & Lackinger, M. (2010). Material- and Orientation-Dependent Reactivity for Heterogeneously Catalyzed Carbon-Bromine Bond Homolysis. *Journal of Physical Chemistry C*, 114 (29): 12604-12609.

Wiesendanger, R. (1994). *Scanning Probe Microscopy and Spectroscopy: Methods and Applications*. First ed. Cambridge: The Press Syndicate of The University of Cambridge.

Woodruff, D. P. & Delchar, T. A. (1994). *Modern Techniques of Surface Science - Second Edition*. Cambridge: The Press Syndicate of The University of Cambridge.

Yoon, J. K., Son, W. J., Chung, K. H., Kim, H., Han, S. & Kahng, S. J. (2011). Visualizing Halogen Bonds in Planar Supramolecular Systems. *Journal of Physical Chemistry C*, 115 (5): 2297-2301.